JGR Solid Earth

RESEARCH ARTICLE
10.1029/2025JB032982

OBS Data Mining Reveals Seismic Structure and Dynamics of the Oceanic Blanco Transform Fault, Northeast Pacific

Cyril Journeau[1,2], Amanda M. Thomas[1,2], Rachel E. Abercrombie[3], Brenton W. Hirao[1], Mingqi Liu[4], and Václav Kuna[5]

[1]Department of Earth Sciences, University of Oregon, Eugene, OR, USA, [2]Department of Earth and Planetary Sciences, University of California, Davis, CA, USA, [3]Department of Earth and Environment, Boston University, Boston, MA, USA, [4]Department of Earth Sciences, University of Southern California, Los Angeles, CA, USA, [5]The Institute of Geophysics of the Czech Academy of Sciences, Prague, Czech Republic

Abstract Deformation along oceanic transform faults is partitioned between seismic and aseismic slip, controlled by lithology, thermal structure, and fluid circulation. We analyze one year of data from a 54-station ocean bottom seismometer network deployed across the Blanco Transform Fault (BTF), Northeast Pacific. Using machine-learning pickers and high-precision location methods, we construct a high-resolution microseismicity catalog with over 30,000 earthquakes. Comparison with three independent catalogs shows that earthquake depth estimates vary with velocity models, phase association, and location strategies. Our enhanced catalog reveals strong along-strike variations in seismicity, including depth extent, density, and moment release. Seismicity concentrates near structural step-overs, which host ∼2.4 times more earthquakes than intervening transform segments, indicating segmentation of the fault system. Four-dimensional spatiotemporal patterns highlight marked contrasts between transforms and step-overs. Extension at step-overs likely enhances fluid circulation within networks of normal faults, sustaining high microearthquake rates and seismic bursts. Comparison with three-dimensional thermal models constrains the nature and thermal state of the BTF step-overs, classifying them as intra-transform spreading centers (ITSCs) or amagmatic pull-apart basins. Along the Blanco Ridge segment, we compare space–time patterns of microseismicity with relocated $M > 5.5$ earthquakes from 1992 to 2019. Three rupture barriers exhibit distinct levels of microearthquake activity, while active seismic bursts in the mantle are concentrated beneath locked M6 patches and one rupture barrier. A crustal northeastward fault bending is observed on the edge of a locked M6 patch. Our results highlight how fault geometry, thermal structure, and fluid-related processes jointly control seismicity patterns and slip behavior on oceanic transform faults.

Plain Language Summary Transform faults are plate boundaries where tectonic plates slide past one another. On land, they can produce damaging earthquakes and also creep slowly without noticeable shaking. They are harder to study in the oceans, yet seismicity records from seafloor seismometers provide a natural laboratory for understanding earthquake behavior and slip modes in rocks with a different rheology than those on land. We investigate the Blanco Transform Fault off the coast of Oregon using machine learning, nearly doubling the number of known small seismic events. This dense catalog shows that earthquakes are not evenly distributed: they mainly cluster where the fault steps sideways ("step-overs") and vary along the main transform segments. Comparison of earthquake patterns with models of temperature suggests that heat flow and seawater circulating through the crust influence where earthquakes occur and how deep they reach. The Blanco Ridge transform segment shows strong changes along its length, with two repeatedly active, stronger patches separated by a barrier zone. Our results suggest that fault architecture, temperature, and fluid–rock interactions jointly control seismicity and influence the balance between rapid earthquake slip and slow fault movement along oceanic transform faults.

Key Points:

- A machine-learning catalog resolves along-strike segmentation, with step-overs hosting 2.4 times more earthquakes than transform segments
- Seismicity compared with different numerical thermal models provide new insights into the nature and thermal state of step-overs
- Blanco Ridge seismicity includes mantle swarms beneath locked M6 patches, barrier zones, and shallow crustal fault bending at one barrier

Supporting Information:

Supporting Information may be found in the online version of this article.

Correspondence to:

C. Journeau,
crjourneau@ucdavis.edu

Citation:

Journeau, C., Thomas, A. M., Abercrombie, R. E., Hirao, B. W., Liu, M., & Kuna, V. (2026). OBS data mining reveals seismic structure and dynamics of the oceanic Blanco Transform Fault, Northeast Pacific. *Journal of Geophysical Research: Solid Earth*, *131*, e2025JB032982. https://doi.org/10.1029/2025JB032982

Received 12 SEP 2025
Accepted 27 MAY 2026

Author Contributions:

Conceptualization: Cyril Journeau, Amanda M. Thomas, Rachel E. Abercrombie
Data curation: Václav Kuna
Formal analysis: Cyril Journeau, Amanda M. Thomas, Rachel E. Abercrombie
Funding acquisition: Amanda M. Thomas, Rachel E. Abercrombie
Investigation: Cyril Journeau, Amanda M. Thomas, Rachel E. Abercrombie, Brenton W. Hirao, Mingqi Liu, Václav Kuna

1. Introduction

1.1. Physical Parameters Shaping the Seismic Structure and Dynamics Beneath Oceanic Transforms

Oceanic transform faults (OTFs) are strike-slip plate boundaries that accommodate horizontal motion between oceanic plates, either linking offset ridge segments or terminating at triple junctions (Fox & Gallo, 1984). Their seismic behavior is strongly influenced by lithospheric age, spreading rate, and the associated thermal structure (Abercrombie & Ekström, 2001; Boettcher & Jordan, 2004). OTFs span a broad range of spreading rates, from

Methodology: Cyril Journeau, Amanda M. Thomas, Rachel E. Abercrombie, Brenton W. Hirao, Mingqi Liu, Václav Kuna
Project administration: Amanda M. Thomas, Rachel E. Abercrombie
Resources: Amanda M. Thomas, Rachel E. Abercrombie, Mingqi Liu, Václav Kuna
Software: Cyril Journeau, Amanda M. Thomas, Brenton W. Hirao, Mingqi Liu
Supervision: Amanda M. Thomas, Rachel E. Abercrombie
Visualization: Cyril Journeau, Amanda M. Thomas, Rachel E. Abercrombie
Writing – original draft: Cyril Journeau, Amanda M. Thomas, Rachel E. Abercrombie
Writing – review & editing: Cyril Journeau, Amanda M. Thomas, Rachel E. Abercrombie, Brenton W. Hirao, Mingqi Liu, Václav Kuna

ultra-slow (<20 mm/yr, e.g., Jan Mayen Transform, Mohns ridge, in the Arctic Ocean) to ultra-fast (>130 mm/yr, e.g., Gofar Transform Fault on the East Pacific Rise), encompassing systems such as the Charlie-Gibbs (20 − 30 mm/yr), Blanco (~ 30 − 60 mm/yr), and Clipperton (>60 mm/yr) transform faults (DeMets et al., 2010). Scaling relationships indicate that spreading rate exerts a first-order control on both maximum earthquake magnitude and recurrence interval, with slower-slipping OTFs generally producing larger earthquakes separated by longer interseismic periods (Boettcher & Jordan, 2004; Boettcher & McGuire, 2009).

Thermal structure is widely recognized as the dominant control on the brittle–ductile transition and, consequently, on the depth extent of seismicity on ocean transform faults (Abercrombie & Ekström, 2001; Behn et al., 2007; Boettcher et al., 2007). Earthquake depth distributions indicate that seismic slip is largely confined to regions cooler than ~600°C, with deeper seismicity occurring where transforms offset older and colder lithosphere (Abercrombie & Ekström, 2001). Laboratory experiments on olivine corroborate this thermal threshold, demonstrating a transition from unstable to stable frictional behavior near 600°C under geologic strain rates (Boettcher et al., 2007). Together, these observations suggest that spreading rate, lithospheric age, and fault rheology collectively govern the thickness of the seismogenic zone and the maximum depth of brittle failure along OTFs.

Despite their large fault areas, OTFs typically exhibit low seismic coupling and release only a small fraction of accumulated plate motion through earthquakes. This apparent seismic deficit has long been attributed to widespread aseismic creep (Abercrombie & Ekström, 2001). Conceptual models proposed by Boettcher and Jordan (2004) span a range of coupling configurations, from uniformly weak faults to systems composed of discrete, fully coupled patches embedded within creeping or weakly coupled regions. Subsequent observations favor the latter scenario, in which large earthquakes rupture isolated asperities bounded by aseismic segments (Boettcher & Jordan, 2004; Wolfson-Schwehr & Boettcher, 2019). Global relocations of $M_W \geq 5.5$ earthquakes further show that creeping segments are ubiquitous on OTFs and commonly occupy more than half of the fault length, indicating strong along-strike variability in seismic coupling (Shi et al., 2022).

Geophysical imaging and dense OBS observations provide direct evidence that this along-strike variability is linked to structural and hydrological heterogeneity within selected transform fault zones. At the Gofar transform fault, seismic velocity and V_p/V_s models reveal low-velocity, fluid-rich damaged zones that separate rupture-prone segments and act as persistent rupture barriers (Roland et al., 2012; Froment et al., 2014; Guo et al., 2018; T. Liu et al., 2023). These features correlate with elevated microseismicity between repeating ~M_w 6 earthquakes and are interpreted as regions of enhanced damage, elevated pore pressure, or complex fault geometry that inhibit dynamic rupture propagation (Fan et al., 2026; Gong & Fan, 2022; Gong et al., 2026; McGuire et al., 2012; Roland et al., 2012; Wolfson-Schwehr et al., 2014). Hydrothermal circulation further modulates fault zone properties by efficiently cooling the lithosphere and altering frictional behavior, exerting a first-order control on seismogenic depth and slip mode (Molnar, 2020; Roland et al., 2010). Recent imaging of conductive anomalies at Gofar provides direct evidence for sustained deep fluid pathways (Chesley et al., 2025).

While these studies highlight the central role of thermal structure, fluids, and fault zone heterogeneity in governing seismic behavior on OTFs, progress has been limited by sparse observations in submarine environments. This limitation can be addressed using dense OBS networks combined with advanced seismic processing techniques to construct high-resolution earthquake catalogs. Recent applications of machine-learning-based phase picking have dramatically lowered magnitude detection thresholds, revealing detailed patterns of microseismicity and slip-mode variability along transform faults (Fan et al., 2026; Gong & Fan, 2022; Gong et al., 2022, 2023, 2026; Lange et al., 2026). Here, we analyze 1 year of data from the X9 OBS deployment across the Blanco Transform Fault (BTF) (Nabelek & Braunmiller, 2012), constructing a high-resolution earthquake catalog by lowering the magnitude of completeness using machine-learning phase picking. Whereas previous detailed studies have focused primarily on fast-slipping systems such as Gofar, our analysis, together with recent work by M. Liu and Tan (2025) and Lange et al. (2026), provides the first comprehensive view of seismicity in an intermediate-rate transform fault, nearly doubling the total length of oceanic transform faults investigated at this level of detail.

1.2. The Blanco Transform Fault Morphology, Seismic and Thermal Structure

The BTF zone (Figure 1) is a ~350 km long oceanic plate boundary that accommodates relative motion between the Pacific and Juan de Fuca plates at intermediate rates of 49–56 mm/yr (Wilson, 1993). It connects the Gorda

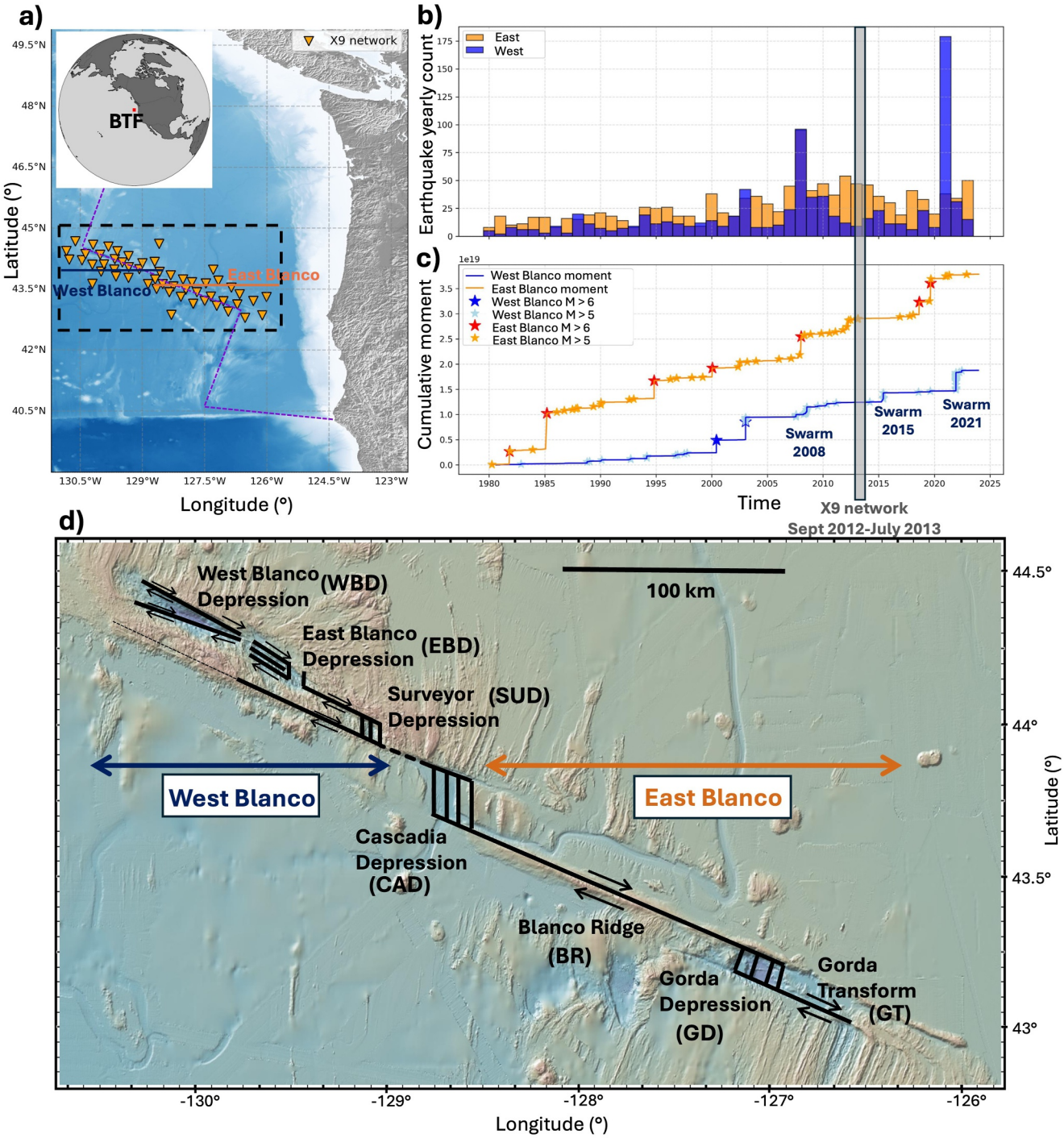

Figure 1. Morphology and seismicity of the Blanco Transform fault system with location of X9 OBS network (2012–2013). (a) Map showing approximative plate boundaries in the offshore Cascadia area. The inverted orange triangles indicate the position of the OBS stations forming the X9 network (2012–2013). Top left insert shows the position of BTF in the Pacific Ocean offshore North America. The black rectangle with dashed lines represent the boundaries of the study area, zoomed in (d). (b) and (c) show the time evolution of the yearly earthquake count, and cumulative seismic moment, respectively for the West Blanco segment (blue) and East Blanco segment (orange). M6 earthquake mainshocks, and M5 earthquake swarms occurring on BTF are reported in (c). (d) Morphology of the BTF system with strike-slip transform fault and pull-apart basins. The map was created using GeoMapApp (https://www.geomapapp.org). Solid black lines represent the Blanco fault and step-overs as mapped in Kuna (2020). The dashed black line represents an aseismic gap between Cascadia Depression and Surveyor Depression.

Ridge to the east and the Juan de Fuca Ridge to the west and is composed of a series of morphologically distinct segments, including extensional basins and transform fault zones (Dziak et al., 1991, 2000; Embley & Wilson, 1992). A clockwise shift in the Juan de Fuca–Pacific pole of rotation around 5 Ma, followed by a series of ridge propagation events, initiated the formation of the BTF system (Ren et al., 2023). The BTF zone is divided into two parts with distinct behavior and morphology: the West Blanco and East Blanco segments, separated by the Cascadia Depression (CAD).

The East Blanco segment comprises two transform segments, Blanco Ridge (BR) and Gorda Transform (GT), separated by a step-over at the Gorda Depression (GD). According to Ren et al. (2023), BR and GT formed at approximately 1.6 Ma and 0.6 Ma, respectively, and together constitute a mechanically mature transform boundary. BR is the longest segment of the system, extending over 100 km. In contrast, the West Blanco segment consists of short, complex transform strands associated with the West Blanco Depression (WBD), East Blanco Depression (EBD), and Surveyor Depression (SUD), with step-overs at EBD and SUD. Seismic slip vectors in this western region are systematically skewed relative to plate motion, suggesting that West Blanco remains an immature plate boundary still adjusting to the current stress regime (Ren et al., 2023). This morphological and kinematic contrast is mirrored by along-strike variations in the depth distribution of seismicity resolved in the 2012–2013 OBS earthquake catalog of Kuna (2020). This suggests that East Blanco has undergone more efficient long-term hydrothermal cooling, deepening the brittle–ductile transition and allowing seismicity to extend deeper into the upper mantle than at West Blanco.

Another fundamental West–East dichotomy along the BTF concerns the long-term cumulative seismic moment release and associated slip modes (Figure 1). The East Blanco segment, particularly along the BR, exhibits a significantly higher rate of $\sim M_w$ 6 earthquakes rupturing two distinct asperities approximately every ~13.5 years (Boettcher & McGuire, 2009; Braunmiller & Nábělek, 2008), indicative of stronger seismic coupling. In contrast, the West Blanco segment has hosted only two $\sim M_w$ 6 earthquakes over the past 45 years, implying substantially lower seismic coupling. Step-overs and pull-apart basins at EBD, SUD, CAD, and GD are systematically associated with reduced seismic moment release and are thought to accommodate a larger fraction of plate motion through aseismic or microseismic deformation (Braunmiller & Nábělek, 2008).

1.3. Step-Overs Seismicity and Thermal Structure

Pull-apart basins represent immature step-overs where mantle flow is predominantly horizontal, resulting in little lithospheric thinning, deep 1,200°C isotherms, and little to no melt reaching the surface. When step-over geometry and spreading rate exceed a critical threshold, extension can instead lead to the development of intra-transform spreading centers (ITSCs) characterized by vertical mantle upwelling, progressive thermal resetting, shallower isotherms, and active or intermittent magmatism (Wolfson-Schwehr et al., 2017). Based on the ratio between step-over length and a critical step-over length, Wolfson-Schwehr et al. (2017) define three thermal regimes: type I step-overs, corresponding to fully developed ITSCs with ridge-like thermal structure; type II step-overs, corresponding to transitional magma-bearing pull-apart basins or immature ITSCs; and type III step-overs, corresponding to magma-poor pull-apart basins with predominantly horizontal mantle flow.

CAD lies at the junction between the East and West Blanco segments and has long been interpreted as a possible ITSC based on its morphology and seismic characteristics (Embley & Wilson, 1992). At CAD, the presence of normal faulting, deep upper-mantle seismicity, and weak positive magnetization suggests that it functions as a magma-poor ITSC with a deep but limited melt source (Braunmiller & Nábělek, 2008; Embley & Wilson, 1992; Ren et al., 2023). Deep seismicity beneath CAD has been interpreted as reflecting intermittent diking episodes that cool rapidly due to efficient hydrothermal circulation, thereby inhibiting sustained magmatism (Kuna, 2020).

Seismotectonic analysis further indicates that among the major step-overs of the BTF, only CAD and GD correspond to active ITSCs, whereas EBD and SUD represent remnant, aborted rift structures that did not evolve into fully developed spreading centers (Ren et al., 2023). Thermo-mechanical modeling by Chen et al. (2025) demonstrates that the presence and distribution of ITSCs exert a first-order control on the thermal structure of the BTF, with multiple ITSCs in the western segment leading to enhanced mantle upwelling and shallower isotherms, whereas the eastern segment, characterized by a single ITSC at GD, retains a colder thermal structure and deeper 600°C isotherm, consistent with the observed asymmetry in maximum earthquake depths along strike.

In this study, we aim to further understand how the space–time organization of microseismicity at step-overs reflects their thermal state and mechanical maturity. Here, we systematically examine the maximum depth and spatiotemporal evolution of seismicity across the major step-overs of the BTF system and compare these observations with multiple thermo-mechanical configurations. This integrated analysis allows us to better constrain the nature, and thermal imprint of individual step-overs along the fault system.

Seismicity along OTFs is generally expected to be confined above the ∼600°C isotherm. However, earthquakes on several systems, including the Blanco, Gofar, and Discovery transform faults, have been reported at depths where temperatures may exceed 750–1,000°C (Molnar, 2020). This apparent discrepancy may reflect brittle failure at higher temperatures than commonly assumed, enhanced hydrothermal cooling that depresses isotherms, or systematic biases in earthquake depth estimates arising from velocity model uncertainties. For example, Grevemeyer et al. (2019) demonstrated that apparently deep seismicity at spreading centers can result from unmodeled sediment cover or lateral velocity heterogeneity. These challenges are particularly relevant along the BTF, where sediment thickness and crustal structure vary markedly between transform segments and pull-apart basins. To address these uncertainties, we apply the spatially variable station correction method (Lomax & Savvaidis, 2022) to refine earthquake depths by accounting for three-dimensional wave-propagation effects. We compare the resulting relocated catalog with those of Kuna (2020), M. Liu and Tan (2024), and Lange et al. (2026) to assess systematic differences across workflows.

1.4. Slip Modes Beneath the Blanco Ridge Transform Segment

Along the BR transform, previous studies proposed that slip is partitioned between a brittle, strongly coupled crust hosting quasi-periodic M6 ruptures and an underlying serpentinized mantle that accommodates plate motion by episodic creep (Kuna et al., 2019). In this model, episodic mantle creep loads the seismogenic crust and activates small brittle asperities in the uppermost mantle, producing frequent microseismic swarms that may modulate the loading and initiation of large earthquakes on overlying crustal rupture patches (Kuna et al., 2019). Building on these observations, M. Liu and Barbot (2026) emphasize that hydrothermal circulation and associated alteration products generate strong lithological and frictional contrasts, including a crustal talc-rich barrier zone between M6 locked patches that promotes rupture segmentation, while serpentinite-rich mantle domains favor swarm-like seismicity through temperature-dependent healing and shear-heating feedbacks.

In this study, we investigate the detailed space–time organization of microseismicity recorded by the 2012–2013 OBS network and relate it to the long-term seismic behavior of the BR segment, using both local observations and historical $M > 5.5$ earthquakes from the global oceanic transform fault catalog of Shi et al. (2022), calibrated with the M_W 5.5 event that occurred on BR in January 2013. This approach allows us to refine the along-strike locations of the two quasi-periodic M6 asperities previously identified on BR (Boettcher & McGuire, 2009) and to delineate the intervening rupture barrier separating them. Our objective is to determine how mantle microseismic bursts are organized in space and time relative to these locked asperities and the intervening barrier, and to assess what this organization reveals about slip partitioning, coupling, and the interaction between mantle creep and crustal seismic rupture along the BR segment.

2. Data and Methods: From Continuous Seismograms to Earthquake Catalog

2.1. X9 OBS Network

During the Blanco Transform Fault OBS Experiment (September 2012 to October 2013) 55 OBS stations were deployed (Nabelek & Braunmiller, 2012). Thirty stations were equipped with broadband seismometers (Güralp CMG3T), while 25 were equipped with short-period instruments (Mark Products L-28LB). All stations recorded seismic data at a sampling rate of 100 samples per second.

2.2. Earthquake Detection Workflow: Phase Picker and Associator

Seismic data from OBS present unique challenges compared to land-based stations, including random sensor orientations, strong ocean-related noise, limited template availability, and periods of very high event rates. These conditions often reduce the effectiveness of standard detection methods such as STA/LTA or template matching. Recent studies have therefore demonstrated the utility of deep-learning models in detecting seismicity recorded by OBS in the noisy submarine environment of transform faults (Gong & Fan, 2022; Gong et al., 2022, 2023), as

well as submarine volcanoes (K. Wang, Waldhauser, Tolstoy, et al., 2024; K. Wang, Waldhauser, Schaff, et al., 2024).

To evaluate the performance of different models, assess their robustness, and generate the most comprehensive microseismicity catalog at the BTF, we apply an ensemble approach to create four distinct configurations of P and/or S picks for each network station. These configurations are derived from three individual models.

We apply two phase-picking models implemented within the PickBlue framework (Bornstein et al., 2024), consisting of deep learning phase pickers trained on a compiled OBS data set from 15 OBS deployments in different tectonic settings, including the BTF. PickBlue is built on the SeisBench machine-learning platform (Woollam et al., 2022) and provides OBS-optimized versions of two widely used neural network architectures: PhaseNet (Zhu & Beroza, 2018) and EQTransformer (Mousavi et al., 2020), hereafter referred to as BluePhaseNet and BlueEQTransformer, respectively. In this study, we deploy both models using their default PickBlue configurations (picks configuration 1 and 2). Among the training data sets used for PickBlue, waveforms from the X9 OBS network are included, corresponding to 144 earthquakes with a total of 2,850 manually picked P phases and 961 S phases (Ren et al., 2023).

To improve microseismicity detection specific to this area, we train a new convolutional neural network (CNN) model, BlancOBS, using 148,291 P-phase picks from several thousand earthquakes in the X9 network catalog of Kuna et al. (2019); Kuna (2020). This model (Picks configuration 3) is designed to enhance sensitivity to low signal-to-noise ratio (SNR) events that may be underrepresented in the global PickBlue training set. Since this model is only trained from P picks, we try a fourth pick configuration where we combine the P picks from the BlancOBS model with the S picks from the BluePhasenet configuration (BlancOBS-BluePhasenet picks configuration 4).

Before deploying the picker on seismic data, we apply a high-pass filter with a cutoff frequency of 1 Hz. After applying the picker, we keep all the P and S-wave picks with a probability higher than 0.1. We then apply the PyOcto associator (Münchmeyer, 2024) to associate the phase detections to an earthquake source. We use a 1D P-wave velocity model obtained from Christeson et al. (2010) and a V_p/V_s ratio of 1.75 during the association stage (Figure S1a in Supporting Information S1). Using the BluePhasenet configuration, a total of 977,560 P and S phases are associated to 51,509 events. Figure S2 in Supporting Information S1 summarizes the earthquake catalog workflow we apply to identify 30,447 earthquakes over the BTF system.

Figure S3 in Supporting Information S1 compares four CNN-based phase-picking configurations on the X9 OBS data. BlancOBS (and the BlancOBS–BluePhaseNet hybrid) adds many extra P picks and boosts gross detections relative to PickBlue models, but many of these additions lack sufficient station coverage and/or reliable S phases and therefore do not yield more well-located events after quality control (see bar annotations in Figure S3 in Supporting Information S1 for exact counts). The spatial patterns of the filtered events are similar across configurations (Figure S4 in Supporting Information S1). For the final catalog used in subsequent analyses, we adopt BluePhaseNet picks, which show slightly higher phase-picking accuracy than EQTransformer in independent benchmarks Münchmeyer et al. (2022); Bornstein et al. (2024).

2.3. Earthquake Location Workflow and Velocity Model Corrections

Our earthquake location workflow combines the computation of travel-time grids, absolute location using a nonlinear grid-search algorithm, and subsequent refinement with source-specific station travel-time (SSST) corrections.

We first generate P and S wave travel-time grids for each OBS station using PyKonal (White et al., 2020). PyKonal solves the eikonal equation with a fast marching method, providing robust travel-time fields from any source to each grid node. The grids are based on the 1D velocity model of Christeson et al. (2010), with station elevations incorporated by defining the zero reference at the deepest instrument (BB480, –4,787 m). These grids form the forward-modeling framework required for earthquake location.

Absolute hypocenters are then determined with the oct-tree grid-search algorithm of NonLinLoc (NLL) (Lomax et al., 2000, 2009), which identifies the best-fitting source locations given the observed arrival times and the precomputed travel-time grids. In the inversion, individual P- and S-phase arrival times are weighted according to their associated pick probabilities provided by the neural network models such that higher-confidence picks exert

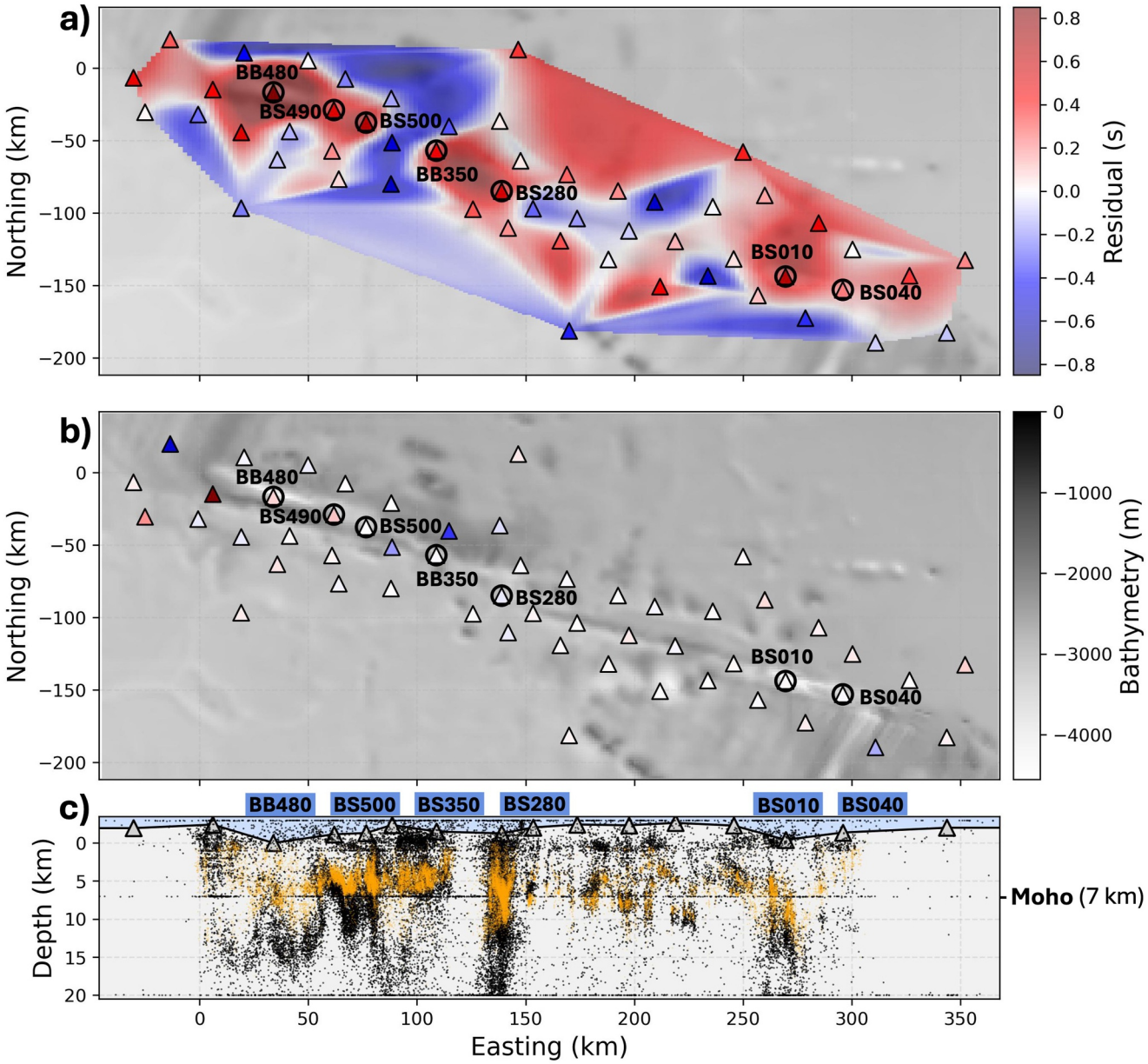

Figure 2. Impact of NLL–SSST corrections on phase residuals and earthquake depth locations. Map of S phase residuals for all stations (denoted by a triangle) (a) before and (b) after relocation with NLL–SSST, respectively. Color bars correspond to residuals (a) and elevation (b). Warm (red) colors indicate positive (late) residuals and cool (blue) colors negative (early). Light gray/white colors highlight negative bathymetric anomalies corresponding to depressions. (c) Easting–depth section along the BTF showing earthquakes located with NLL (black, without station corrections) and the corresponding relocation (orange), illustrating reduced scatter, sharper clustering, and absolute depth corrections after applying SSST. A vertical exaggeration of 3.5 is applied in (c). Earthquakes located above the BB480 station elevation (−4,787 m, our zero depth reference) have a negative depth.

a stronger influence on the final location. Finally, we refine locations using the NLL-SSST approach (Lomax & Savvaidis, 2022), which iteratively derives source- and station-specific travel-time corrections. This method compensates for unmodeled velocity heterogeneity by smoothly adjusting travel times in three dimensions and applying progressively reduced Gaussian spatial smoothing. We calculate the corrected travel-time grids for each station using a subset of 15,000 earthquakes with a local magnitude (M_L) $\geq$ 2, and then relocate the full catalog with these updated grids. Independent benchmarking has shown that NLL-SSST reproduces ground truth depth locations with accuracy comparable to that of relative location algorithms (Yu et al., 2024).

Figure 2 compares earthquake locations before and after applying the NLL-SSST relocation to the BluePhaseNet pick set. The revised locations are spatially more concentrated, reflecting a marked improvement in both horizontal and vertical precision (Figure S5 in Supporting Information S1). This gain arises in part from SSST's ability to correct for lateral variations in seismic velocities, which are not accounted for in the 1D velocity model used here and in previous studies. The most significant adjustments occur beneath sediment-filled basins, where the deepest earthquakes are relocated 3–5 km shallower. These sedimentary layers, which can exceed several hundred meters in thickness and exhibit very low S-wave velocities (< 1 km/s) (Kuna & Nábělek, 2021; Straume et al., 2019), are not represented in the 1D velocity model used here. As a result, they significantly reduce seismic wave speeds and impact both travel-time residuals and depth estimates (Grevemeyer et al., 2019). Moreover, the SSST application corrected the tendency for eathquakes to be located on the strong velocity contrast at the Moho depth (7 km) seen in the original NLL locations without iterations and station corrections (Figure 2c).

Residuals plotted before SSST corrections show that stations above sedimentary basins consistently register large positive P- and S-wave residuals (Figure 2 and Figure S6 in Supporting Information S1), while those residuals are closer to zero after the SSST corrections. This pattern suggests unmodeled low-velocity structures beneath those stations. While the corrected earthquake locations obtained with NLL-SSST are not absolutely correct, they significantly enhance the overall precision of the catalog. This improvement, in turn, increases the clarity and resolution of seismic and aseismic asperities and spatio-temporal patterns along the BTF between 2012 and 2013. We note that some residuals remain uncorrected in the western BTF. Thus, in the sections that follow we focus our interpretation of maximum earthquake depths on the four step-overs (EBD, SUD, CAD, GD) and on BR.

To validate the presence of seismicity that remain in the upper mantle after applying the SSST corrections, we manually inspect some waveforms from events located within a 4 km radius beneath four different stations (BB480, BS500, BS280, and BS010), sampling WBD, EBD, CAD, and GD, respectively (Figure S7 in Supporting Information S1). P-wave arrivals are consistently vertically aligned, while S-wave arrivals exhibit time shifts correlated with depth. This increase in the S-P delay with depth suggests that upper-mantle earthquakes are real and not just a bias linked to the earthquake location method.

2.4. Local Magnitude Estimation

Once an earthquake is detected and located, we estimate an approximate local magnitude (M_L) using the ObsPy Python package (Beyreuther et al., 2010), following the formulation of Bakun and Joyner (1984) developed for Central California. In this approach, peak-to-peak amplitudes are first measured on the horizontal components, after which the instrument response is removed and the amplitudes are converted to equivalent zero-to-peak displacement amplitudes A of a Wood–Anderson seismograph. M_L is then estimated following log–linear regression:

$$M_L = \log_{10} A + a \log_{10} (R/100) + b\,(R - 100) + c, \tag{1}$$

where R is the hypocentral distance (in km), $a = 1$, $b = 0.00301$ and $c = 3$. The constants a, b, c are specific to the California region, nonetheless, Schlaphorst et al. (2023) showed that the California attenuation relations (Bakun & Joyner, 1984; Hutton & Boore, 1987) fit OTF data.

Amplitudes are measured within a 5 s window starting at the S–wave arrival, in order to capture the S–wave maximum while minimizing coda contamination and avoiding interference from other events. A phase pick (P or S) is considered valid if its associated probability exceeds 0.25. If a valid S–phase pick exists, it is used to define the start of the amplitude window. If no valid S–phase pick is available but a valid P–phase pick exists, the S–wave arrival time is predicted from the P–phase pick and the source–station distance, as illustrated in Figure S1b of the Supporting Information S1. Stations without a valid S or P pick are excluded from the M_L estimation. The resulting attenuation curves are shown in Figure S8 in Supporting Information S1. Further work will be required to develop a new local magnitude scale that better captures the attenuation characteristics of the oceanic crust surrounding the BTF zone.

We then calibrate our relative M_L values using seven centroid moment tensor (gCMT) solutions available during the 2012–2013 OBS deployment, under the assumption that $M_L = M_W$ in the range 3–7 (Hanks & Kanamori, 1979). Comparison between the initial M_L estimates obtained from Equation 1 and the corresponding M_W

values indicates that M_L is underestimated by 0.35 magnitude units on average. We therefore recalculate all M_L values by applying this correction directly in Equation 1, using $c = 3 + 0.35$.

We then compute the frequency-magnitude distribution of our catalog and apply the maximum curvature approach (Wiemer & Wyss, 2000) to estimate the magnitude of completeness. We estimate the b-value for different spatial areas of the seismic catalog using the maximum likelihood method (Aki, 1965; Bender, 1983) (Figure S9 in Supporting Information S1).

To characterize along-strike variations in cumulative seismic moment through time, we assume that $M_L = M_W$, and follow the formulation of Hanks and Kanamori (1979) to estimate the approximate seismic moment of each event. In practice, the relationship between M_L and seismic moment deviates systematically at small magnitudes due to the combined effects of source radiation and attenuation at the frequency ranges in which each is measured (Deichmann, 2017; Hanks & Boore, 1984). This results in a systematic underestimation of seismic moment for the smallest events. Nevertheless, because our analysis focuses on relative spatiotemporal variations rather than absolute moment values, this bias does not affect the main conclusions.

2.5. Quality Analysis of the Earthquake Catalog

To assess the robustness and reliability of earthquake detections, we apply a multi-criteria quality control procedure designed to retain only high-confidence events in the final catalog. We use the quality factor $\left(q_f\right)$ introduced by Michele et al. (2019), which provides an objective, normalized measure of earthquake detection and location quality by combining multiple correlated uncertainty estimators into a single scalar metric. The eight combined metrics (RMS, 2D and 3D location errors, azimuthal gap, SNR, averaged P and S probability pick, and total number of picks per earthquake) are shown in Figures S10 and S11 in Supporting Information S1, before and after normalization, respectively. The obtained quality factor (Figure 3f) ranges from 0 (best quality) to 1 (worst quality). Based on this metric, we classify 18,576 events as Class A with $q_f < 0.25$, and 23,434 events as Class B with $0.25 < q_f < 0.40$. In the following analyses, we consider both classes to improve sampling of the lower-magnitude range of the catalog and extend the analysis toward smaller events. However, Class B events are associated with larger uncertainties and are therefore interpreted with greater caution compared to the more robust Class A subset.

To ensure spatial and phase robustness, three additional criteria are imposed (Figures S12b–S12d in Supporting Information S1). First, at least 60% of the stations contributing picks to a given event must belong to the ten closest stations to the earthquake hypocenter, ensuring adequate local azimuthal coverage. Second, at least 60% of contributing stations must have pick probabilities exceeding 0.25, reducing the influence of low-confidence phase detections. Third, at least 60% of the contributing stations must provide an S-phase pick, improving depth resolution and overall location stability. Events failing any of these criteria are excluded from the final catalog. After applying those criteria, we retained 16,750 class A and 13,697 class B earthquakes. Earthquake rejection rates under different criteria are shown in Figure S13 in Supporting Information S1.

Figures 3a–3d illustrate the different stages of filtering out P and S picks and associated earthquakes from the raw BluePhaseNet pick data set to our final catalogs. Figure 3e shows the spatial distribution of our retained class A and class B earthquakes along the BTF. Regarding the Juan de Fuca and Gorda Ridges, only 39 and 44 class B earthquakes are detected, while 285 and 266 earthquakes are present in the class C category, respectively. While our class A BTF earthquake catalog is similar in size and magnitude of completeness to the catalogs of M. Liu and Tan (2024); Lange et al. (2026), including class B events allows us to lower the magnitude of completeness to $M_c = 1.75$, resulting in a total of 30,447 earthquakes (Figure 3g).

2.6. Comparing Seismogenic Thickness Variations From Different Earthquake Depth Estimation Workflows

After correcting the earthquake depth of our catalog, we compare the along-strike variations of maximum earthquake depth with three independent catalogs: those of Kuna (2020), M. Liu and Tan (2025), and Lange et al. (2026) (Figure S14 in Supporting Information S1). All four catalogs reveal a similar first-order segmentation of the BTF. Seismicity tends to be mainly crustal in the western segments while deeper mantle seismicity is more frequent in the eastern segments. CAD stands out as one of the deepest portions of the BTF in all data sets.

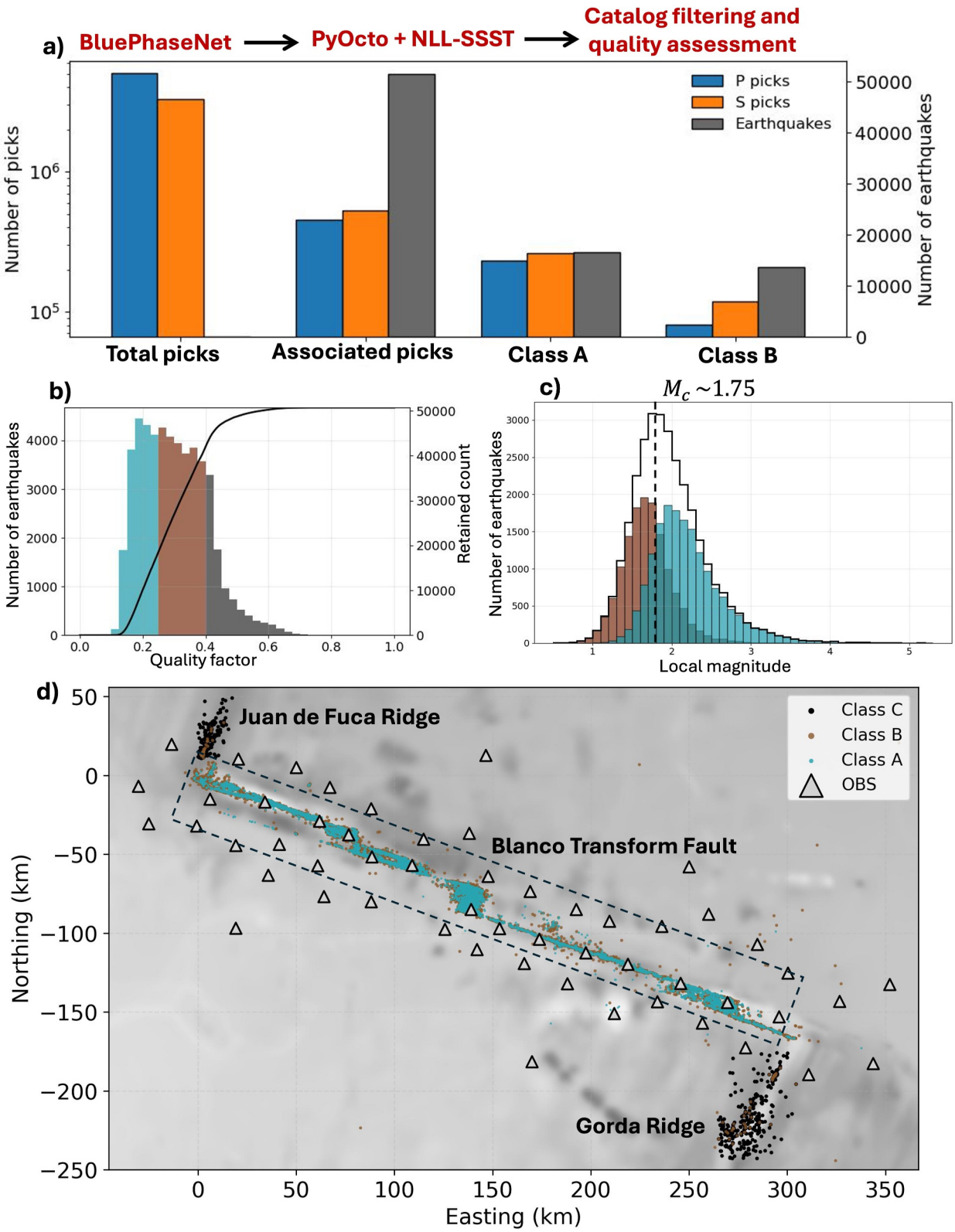

Figure 3.

Despite these general agreements, several regional discrepancies emerge. At BR, we find that spatial clusters of upper-mantle seismicity are shallower than in the catalogs of Kuna (2020) and Lange et al. (2026), while our results are in agreement with the depths of M. Liu and Tan (2025). In other catalogs, GD remains largely crustal whereas our relocations place the eastern GD seismicity in the upper-mantle. While CAD consistently emerges as a deep-seismicity segment, our relocated depths place its maximum at around 13 km, slightly shallower than in the catalogs of Kuna (2020) and M. Liu and Tan (2025), but deeper than the ∼10 km estimate reported by Lange et al. (2026).

Differences in absolute earthquake depths and vertical seismicity patterns highlight the strong influence of initial velocity model assumptions, especially for the shallow structure, as well as the methodologies used for pick-earthquake association, event location, and residual correction. We interpret the 95th percentile earthquake depth as a proxy for the base of the seismogenic zone, but emphasize that such metrics are not purely observational. They are shaped by workflows that vary across studies. Any inference regarding brittle-ductile transitions and thermal structure should therefore consider the intrinsic methodological uncertainties.

We used ChatGPT (OpenAI) solely for language editing and to improve text clarity and structure.

3. Results

3.1. Spatial Distribution of Seismicity on the BTF

3.1.1. Along-Strike Variability of Earthquake Density and Seismic Moment

Figure 4 shows the locations of earthquakes within our high-resolution seismic catalog (30,447 events) and 3D spatial variability along strike. The seismicity is well aligned with the morphological features of the system and reveals a strongly segmented pattern. Spatially distinct segments reflect the seven main substructures of the BTF system: WBD, EBD, SUD, CAD, BR, GD, and GT, see Table 1. Most of the microseismicity (70%, with 21,239 detections) is concentrated beneath the different step-overs of the system (EBD, SUD, CAD and GD). CAD is the most seismically active individual segment with 7,299 detections. Approximately 50% of the seismicity occurs in the West Blanco region, comprising WBD, EBD, and SUD, twice the total number of events detected in East Blanco (BR, GD, GT) with 7,756 detections.

Most of the earthquakes are located in the crust (the majority between 2.5 and 7 km) while about 23% are in the mantle, mainly between 7 and 13 km (Figures S15e and S15f in Supporting Information S1). The seismicity in West Blanco is predominantly crustal (∼88% of events), with an average b-value = 0.95. In contrast, East Blanco shows a higher proportion of mantle seismicity (∼38%), and has a higher average b-value = 1.20. In the CAD, the crust-mantle seismicity distribution is about 67%–33%, and the b-value = 1.13.

In term of cumulative seismic moment, West and East Blanco segments produce a similar amount when averaged over 2012–2013 (Figure S16 in Supporting Information S1). In the West segment, the main part of the seismic energy is released by a long-lasting seismic sequence in EBD in October 2012. In the East segment, the main part is released by BR, the most energetic segment of the system, that hosted a M_W 5.5 event in January 2013.

3.1.2. Calibrating Long-Term 1990–2019 $M > 5.5$ Catalog

To place our short-term OBS observations in a longer-term context, we use the globally relocated catalog of $M_w \geq 5.5$ earthquakes compiled by Shi et al. (2022), which provides systematically corrected epicentral locations for major events on oceanic transform faults worldwide. We extract the subset of events occurring along the BTF for the period 1992–2019 and compare it with our high-resolution OBS-derived catalog. One $M_w \approx 5.5$

Figure 3. OBS earthquake catalog construction and quality assessment. (a) Number of P picks (blue), S picks (orange), and associated earthquakes (gray) at successive stages of the processing workflow. From left to right are shown: the total phase picks produced by the BluePhaseNet picker (5,053,651 P and 3,302,753 S), the phase picks (454,237 P and 523,323 S) successfully associated into 51,509 events using PyOcto and located with NonLinLoc–SSST, the phase picks (230,082 P and 261,311 S) from 16,750 quality-controlled Class A earthquakes, and the phase picks (80,747 P and 118,099 S) from 13,704 quality-controlled Class B earthquakes. Bar labels indicate the number of retained events at each stage. (b) Distribution of location quality metric q (best = 0, worst = 1) for Class A, Class B and Class C earthquakes, with the cumulative distribution shown by the black curve. (c) Magnitude–frequency distributions for retained Class A and Class B catalogs. (d) Map view of the final relocated earthquake catalog along the BTF, showing the Class A (teal) and Class B (brown) events together with OBS station locations (gray triangles) and some Class-C earthquakes on the ridges.

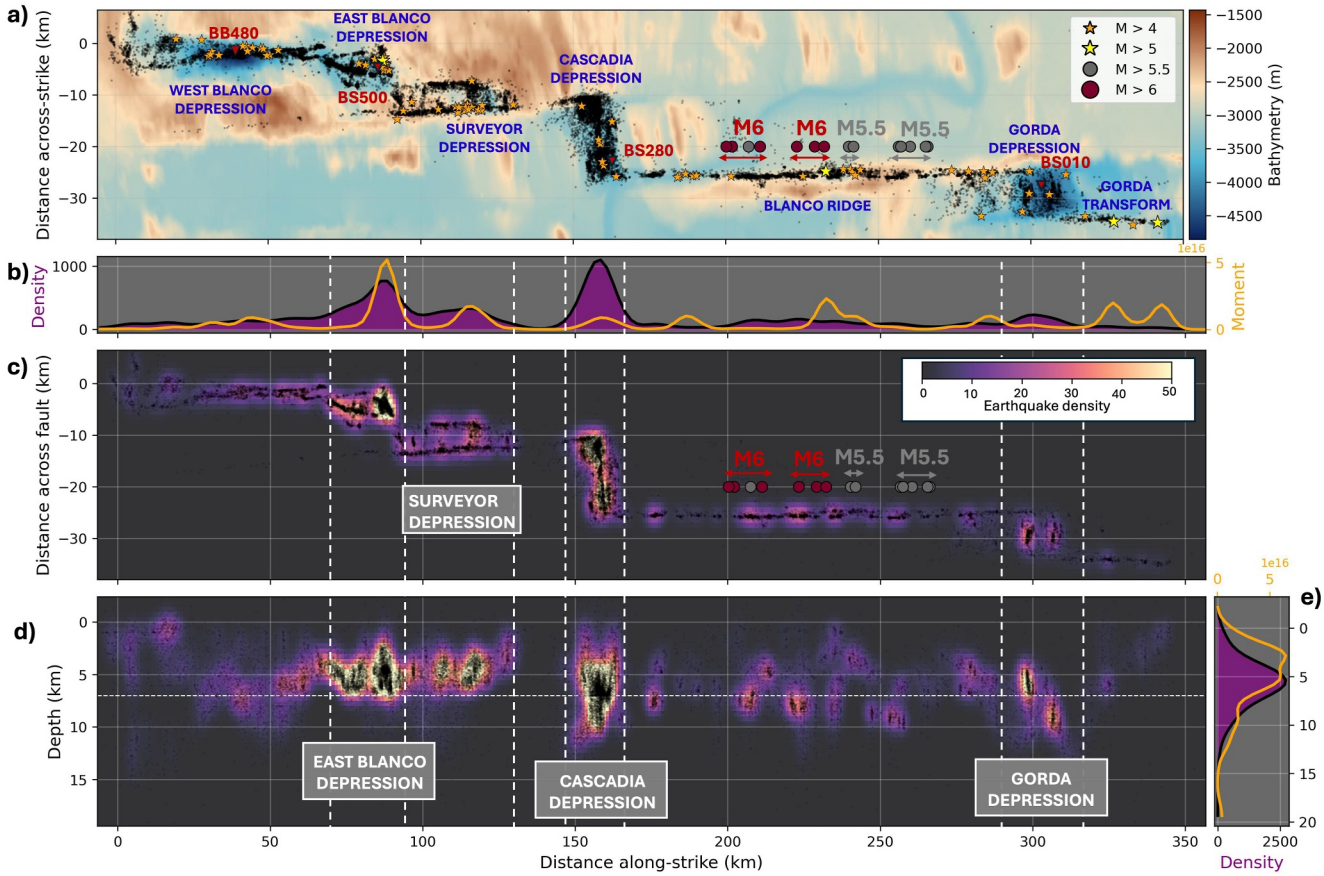

Figure 4. Along-strike segmentation of Blanco fault system and earthquake catalog variations (a) Along-strike vs. across-strike projection of high-resolution seismic catalog on top of bathymetric map, (b) Along-strike variation of the earthquake density (purple filled curve) and spatial seismic moment integral (orange curve). (c) Map representing the 2D (along-strike distance against across-strike distance) variations of the earthquake density. (d) Same as (c) with 2D along-strike against depth variations. The four step-over of BTF (EBD, SUD, CAD, and GD) are highlighted with gray rectangles. A vertical exaggeration of 3.5 is applied in (d). (e) Same as (b) but along-depth.

earthquake on the BR segment, occurring in January 2013, is common to both data sets, allowing us to calibrate the along-strike position of the BR section of the Shi et al. (2022) catalog (Figure S18 in Supporting Information S1). As a result, the spatial alignment of $M_w \geq 5.5$ earthquakes is robustly constrained only for the BR segment, whereas larger uncertainties remain for West Blanco, where no overlapping events are available for calibration. Consequently, $M_w \geq 5.5$ earthquakes on West Blanco are not interpreted further in this study.

Table 1
Event Count, Percentage of Earthquakes in the Crust and Mantle, b-Values, and Cumulative Seismic Moment for Each Region

Region	Event count	Crust (%)	Mantle (%)	b-value	Cumulative moment (Nm)
West Blanco Depression	4,138	75.4	24.57	1.00	1.02×10^{17}
East Blanco Depression	6,289	96.7	3.3	0.90	2.25×10^{17}
Surveyor Depression	4,895	92.6	7.4	1.18	1.16×10^{17}
Cascadia Depression	7,299	66.9	33.1	1.13	5.53×10^{16}
Blanco Ridge	4,456	53.6	46.4	1.18	2.00×10^{17}
Gorda Depression	2,756	56.9	43.1	1.16	8.06×10^{16}
Gorda Transform	544	75.4	24.6	1.02	1.64×10^{17}

Along the BR segment, the calibrated $M_w \geq 5.5$ catalog reveals that $M_w \approx 6$ earthquakes cluster into two spatially persistent patches separated by an along-strike gap without large-event moment release (Figures 4a and 4c). This gap coincides with the location of a long-lived rupture barrier. Two others $M_w \approx 5.5$ earthquakes clusters are located further southeast on BR.

3.2. Relationship Between Blanco Thermal Structure and Spatial Distribution of Seismicity

3.2.1. 3D Numerical Thermal Model

We determine the thermal architecture of the BTF using a 3D thermo-mechanical model (M. Liu et al., 2022; M. Liu et al., 2025; M. Liu & Barbot, 2026), which combines finite differences on a fully staggered Eulerian grid with marker-in-cell techniques. The effective strength of the oceanic lithosphere is governed by a visco-plastic rheology that fully couples brittle/plastic strain-dependent weakening of cohesion and friction coefficient, as well as grain-size evolution for mantle rocks. The oceanic spreading process is implemented through four simplified key processes (M. Liu et al., 2022; M. Liu et al., 2025): (a) spontaneous accretion of mantle lithosphere at the base of the plate; (b) melt production and extraction during mantle decompression melting and transport toward the ridge to form crustal magma reservoirs; (c) cooling and crystallization of melt along the walls of lower-crustal magma reservoirs; and (d) rapid cooling of the shallow oceanic lithosphere via enhanced thermal conductivity using a simplified, temperature- and depth-dependent parameterization of hydrothermal circulation (see Text S1 in Supporting Information S1 for details).

Our approach focuses on characterizing the first-order thermal structure associated with the present-day geometry and kinematics of the BTF. Accordingly, we prescribe an initially uniform, 330-km-long transform fault with realistic plate ages and a full spreading rate of 49 mm/yr, while simplifying the BTF geometry by neglecting the intra-transform features (e.g., extension basins, short spreading centers). The simulation reaches a quasi-steady-state thermal regime following 1.5 Myr of evolution (Figure S19 in Supporting Information S1). We then derive the along-fault thermal profile by tracking the maximum temperature within the transform deformation zone and compare this profile with the observed seismicity. We apply a factor 1.05 to the thermal model so that it matches the real size of BTF ($\sim$347 km).

This approach implicitly assumes that, despite ongoing evolution of the BTF (Embley & Wilson, 1992; Ren et al., 2023), the present-day configuration has persisted long enough at depth for the thermal field within the transform deformation zone to become largely insensitive to the imposed initial conditions and to reflect the dominant controls of spreading, shear heating, and hydrothermal circulation. Nevertheless, even simplified thermos-mechanical models can provide an idealized, end-member representation of the BTF thermal structure to constrain the relationship between transform deformation zone temperature, rheology, and seismicity (Roland et al., 2010).

3.2.2. Comparison Between Thermal Structures and Maximum Earthquake Depth

We compare observed earthquake depths with predicted brittle–ductile transition ($\sim$600°C) depths from multiple thermo-mechanical models along BTF (Figure 5). The maximum depth of seismicity is quantified using the 95th percentile of earthquake depths computed within over 1-km sliding along-strike windows. This metric is used consistently to evaluate agreement between observed seismicity and modeled 600°C isotherms.

In the BTF-calibrated model developed in this study assuming no ITSC (0 ITSC; Figure 5a), the predicted 600°C isotherm closely follows the observed maximum earthquake depths along most of the fault, indicating that nearly all seismicity occurs within the modeled brittle domain. Departures from this pattern are limited to WBD and locally at GD, where a small number of events reach or slightly exceed the 600°C isotherm. In contrast, the 0 ITSC configuration of Chen et al. (2025) places the 600°C isotherm systematically deeper than the observed seismicity envelope (Figure 5b), overestimating the depth extent of brittle deformation.

Introducing ITSCs in the models of Chen et al. (2025) results in progressively improved agreement with the observed seismicity envelope. The 1 ITSC configuration shifts the 600°C isotherm upward toward the 95th percentile depths (Figure 5c), while the 4 ITSC configuration reproduces several along-strike variations in maximum earthquake depth (Figure 5d). In particular, this configuration captures shallower seismicity in West Blanco, where two potential ITSCs are present (at EBD and SUD), and deeper seismicity in East Blanco, where only one potential ITSC is inferred at GD.

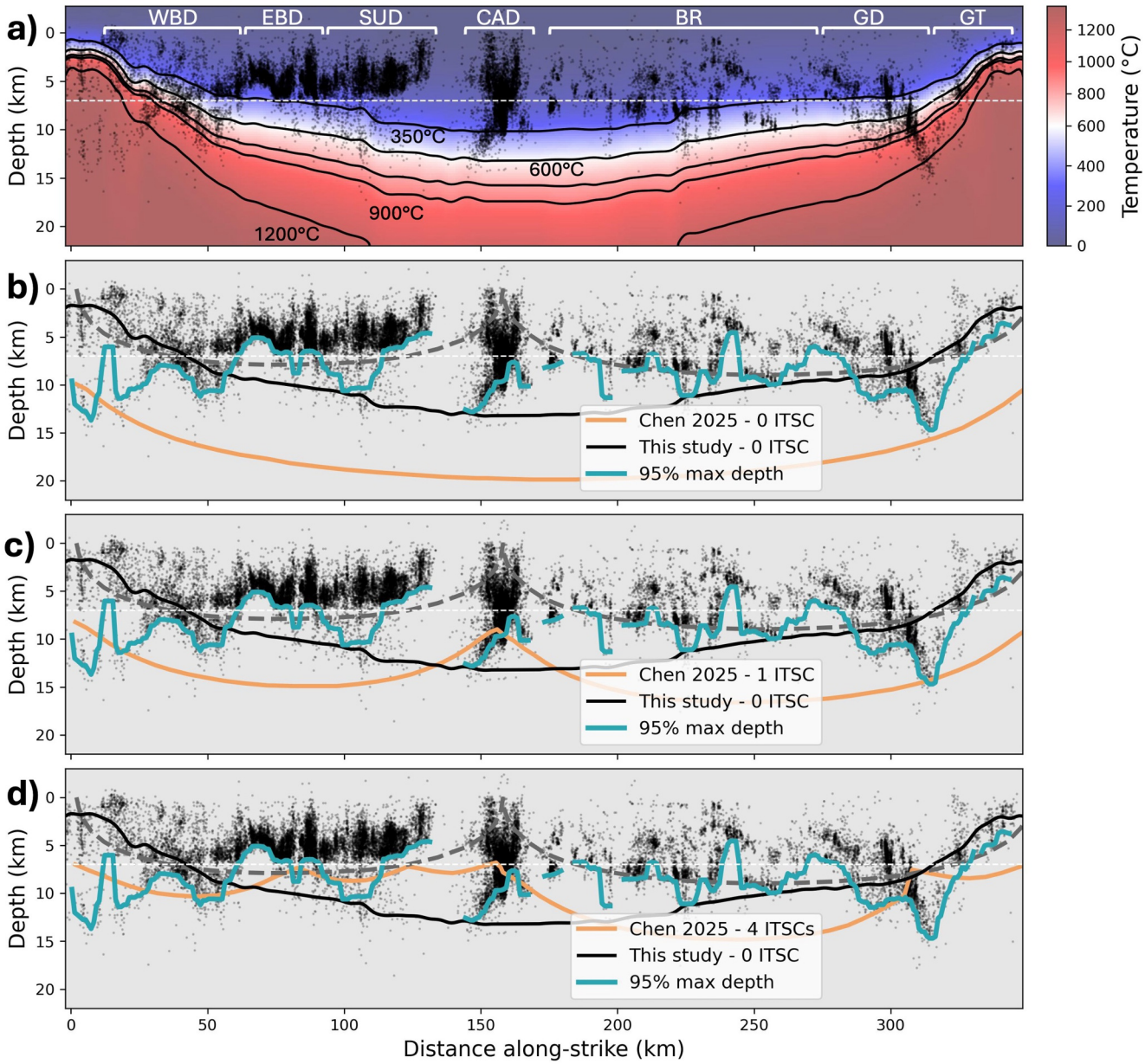

Figure 5. Along-strike thermal structure and depth distribution of seismicity along the Blanco Transform Fault. (a) Along-strike cross-section of the BTF showing the spatial distribution of earthquakes (black dots) overlaid on the temperature field of our BTF-calibrated thermo-mechanical model. Black contours indicate selected isotherms (350°C, 600°C, 800°C, 900°C, and 1,200°C). (b)–(d) Comparison between observed maximum earthquake depths and alternative thermal configurations. Black dots show earthquake hypocenters projected along strike. The turquoise curve represents the 95th percentile of earthquake depth computed within 1 km sliding along-strike windows. The black curve corresponds to the 600°C isotherm predicted by our BTF-calibrated model (This study—0 ITSC configuration). Orange curves show the 600°C isotherm predicted by the thermo-mechanical models of Chen et al. (2025) assuming (b) zero intra-transform spreading centers (0 ITSC), (c) one ITSC, and (d) four ITSCs distributed along the fault. Gray dashed curves indicate the half-space cooling model assuming a central ITSC. In (a), (b), (c) and (d), the horizontal white dashed line stands for the Moho, and a vertical exaggeration of 3.5 is applied.

3.3. Along-Strike Variations of Spatio-Temporal Seismic Patterns

Along-strike spatial contrasts reveal differences in the 3D distribution of seismicity. In the western part of the system, activity is more spatially continuous along transform segments separated by the EBD and SUD step-overs. Eastward, particularly beneath the BR segment, seismicity becomes more spatially clustered and mantle events are more frequent, forming concentrated patches separated by relatively quiescent or aseismic stretches.

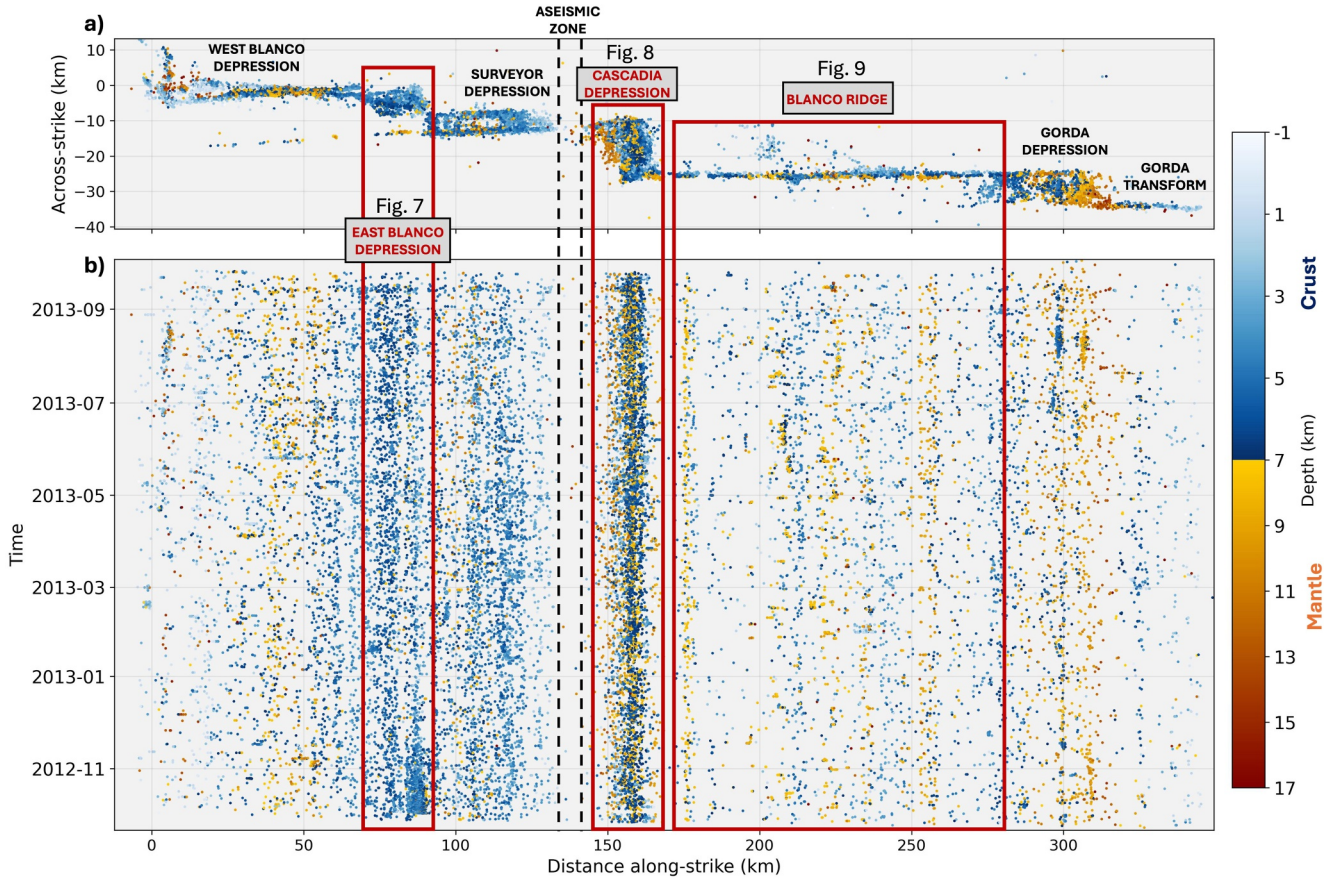

Figure 6. Blanco segmentation and along-strike variability of the spatio-temporal patterns. (a) Map of the seismic catalog projected in the along-strike and across-strike directions. (b) Time evolution of the along-strike projection of the catalog. The light blue to dark red colorbar in (a) and (b) represent the earthquake depth. Red rectangles in (b) highlight the areas where zoom are provided in Figures 7–9.

Figure 6 illustrates along-strike variability in earthquake depth (crust vs. mantle) and spatiotemporal distribution, showing that temporal behavior covaries with the spatial contrasts. BR is dominated by intermittent space–time clusters, crustal mainshock–aftershock sequences and deeper mantle swarms (Kuna et al., 2019). In contrast, the step-overs (EBD, SUD, CAD, GD) exhibit sustained background activity that is nearly continuous in space–time, with space-time clusters occasionally superposed.

3.3.1. Spatio-Temporal Seismic Patterns at Step-Overs

To illustrate the diversity of seismic behavior at step-overs along the BTF, we present detailed space–time views of seismicity at two representative structures: EBD in West Blanco and the CAD. For each step-over, we examine the three-dimensional spatial distribution of earthquakes, their magnitude distribution, and their temporal evolution during the OBS deployment.

At EBD, seismicity forms several spatially distinct clusters distributed along strike (Figures 7a, 7c, and 7d). Most seismicity is concentrated in the crust, with a few hundred events occurring in the upper-mantle beneath the eastern part of the EBD. The magnitude (Figures 7b, 7d, 7e and 7f) and seismic moment (Figure S17b in Supporting Information S1) distributions show that most seismic moment during the OBS period was released during a single intense seismic swarm in October 2012, at the onset of the deployment, which includes the largest events observed at this step-over. Additional, smaller seismic bursts are visible throughout the observation period in the time–space projections (Figures 7e and 7f), indicating recurrent episodes of elevated seismic activity superimposed on lower background rates.

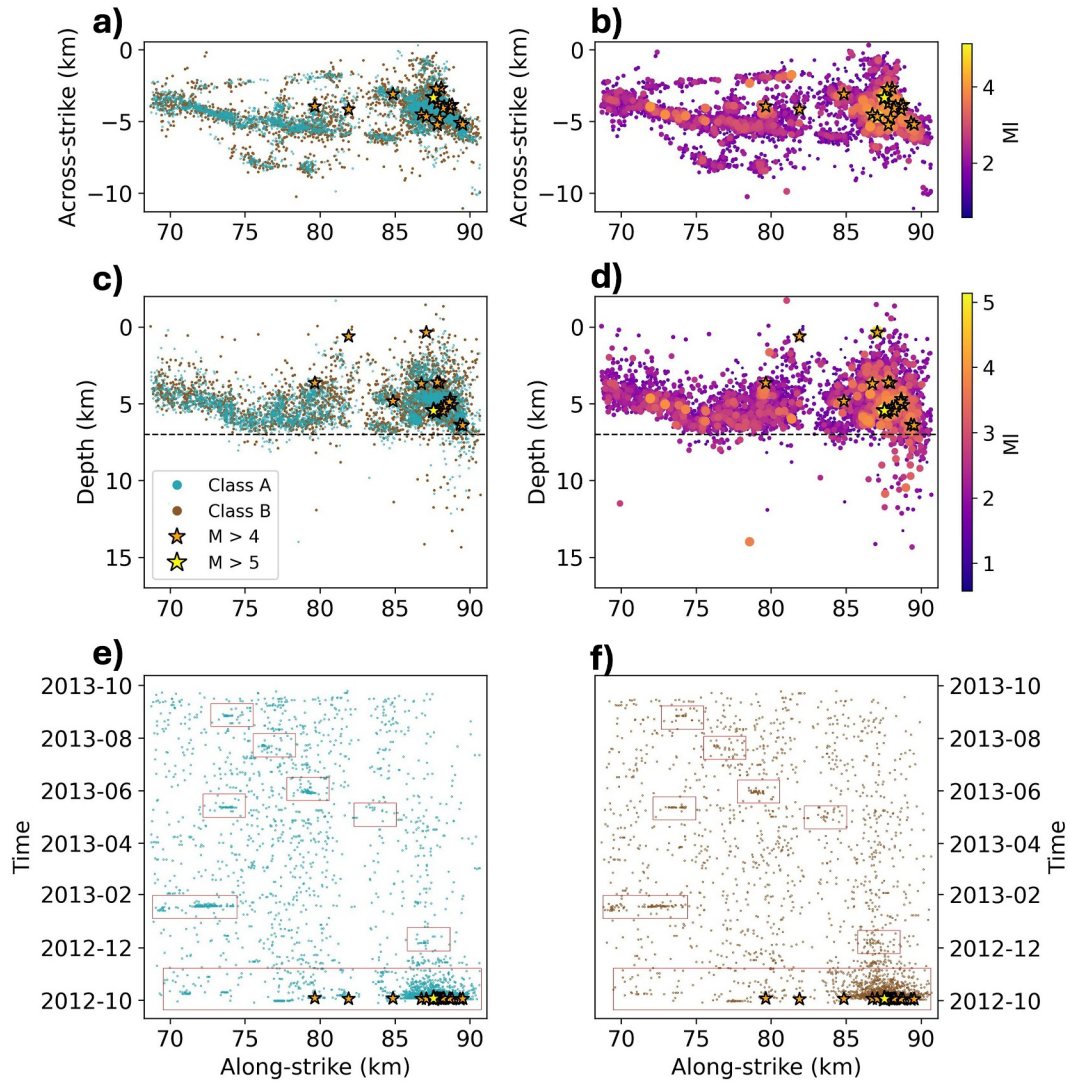

Figure 7. Space–time distribution of seismicity at EBD step-over. (a) Map view of earthquakes showing across-strike vs. along-strike position. Teal blue and brown colors distinguish Class A and B events, respectively. Orange and yellow stars indicate $M > 4$ and $M > 5$ earthquakes, respectively. (b) Same view as (a), with symbol color and size scaled by local magnitude (M_l) (c) Along-strike vs. depth projection of seismicity. (d) Same view as (c), with symbol color and size scaled by local magnitude (M_l). Horizontal black dashed line stand for the Moho in (c) and (d). (e) Time vs. along-strike distribution of Class A earthquakes over the OBS deployment period, showing some temporal clustering and swarm activity within the red rectangles. (f) Same as (e) for Class B earthquakes.

Seismicity at CAD also exhibits pronounced clustering in both space and time (Figure 8). Earthquakes are distributed across multiple along-strike clusters, with seismicity extending deeper than at EBD, reaching mantle depths of up to ∼13 km in the northern portion of the system (Figures 8c and 8d). The magnitude-scaled view (Figure 8b) indicates the absence of $M > 5$ earthquakes during the OBS deployment, despite sustained seismic activity and seven $M > 4$ occurrence. Time–space projections (Figures 8e and 8f) show that seismicity at CAD is dominated by repeated episodic seismic bursts superimposed on continuous activity.

3.3.2. Spatio-Temporal Seismic Patterns Blanco Ridge and Long-Term 1980–2026 $M > 5.5$ Earthquakes

In Figures 9a–9c, we compare the spatiotemporal organization of the short-term microseismic activity along BR with the long-term $M_w \geq 5.5$ earthquakes occurrence. Two distinct along-strike clusters of $M_W \sim 6$ earthquakes are evident in the long-term catalog, each coinciding with regions of dense microseismicity observed during the OBS deployment. Beneath these patches, seismicity extends into the upper mantle and forms elongated clusters

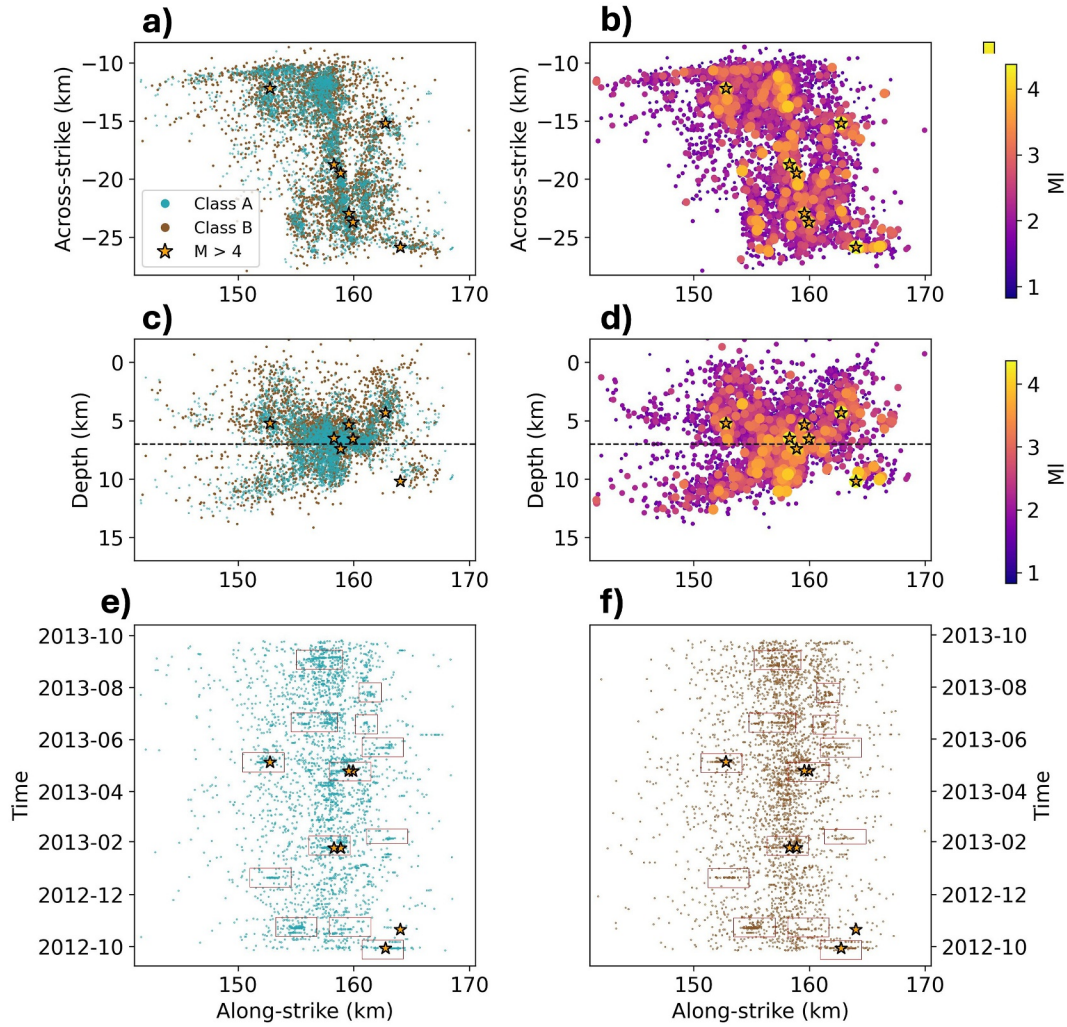

Figure 8. Space–time organization of seismicity along the Cascadia Depression. (a) Map view of earthquakes showing across-strike vs. along-strike position. Teal blue and brown colors distinguish Class A and B events, respectively. Orange and yellow stars indicate $M > 4$ and $M > 5$ earthquakes, respectively. (b) Same view as (a), with symbol color and size scaled by local magnitude (M_l) (c) Along-strike vs. depth projection of seismicity. (d) Same view as (c), with symbol color and size scaled by local magnitude (M_l). Horizontal black dashed line stand for the Moho in (c) and (d). (e) Time vs. along-strike distribution of Class A earthquakes over the OBS deployment period, showing some temporal clustering and swarm activity within the red rectangles. (f) Same as (e) for Class B earthquakes.

that migrate in space and time (Kuna et al., 2019). In contrast, the ∼10 km-wide along-strike interval separating the two $M_W \sim 6$ patches exhibits markedly reduced seismicity at mantle depths, defining a comparatively quiet rupture barrier in the short-term catalog. To the northwest of this barrier, however, a spatial cluster of crustal microseismicity remains almost continuously active.

East of the eastern $M_W \sim 6$ patch, a second transition zone separates this asperity from a $M_W \approx 5.5$ rupture patch. Unlike the central barrier, this zone hosts active deep seismicity, including clustered mantle earthquakes reaching depths of ∼10–12 km (Figures 9b–9d). The across-strike and depth projections further show a systematic northeastward offset of seismicity of approximately 1.5 km across this transition (Figure 9c), indicating a localized change in fault geometry coincident with enhanced deep seismic activity. These observations highlight distinct spatial expressions of rupture barriers along BR, ranging from seismically quiet zones to regions characterized by active deep swarming.

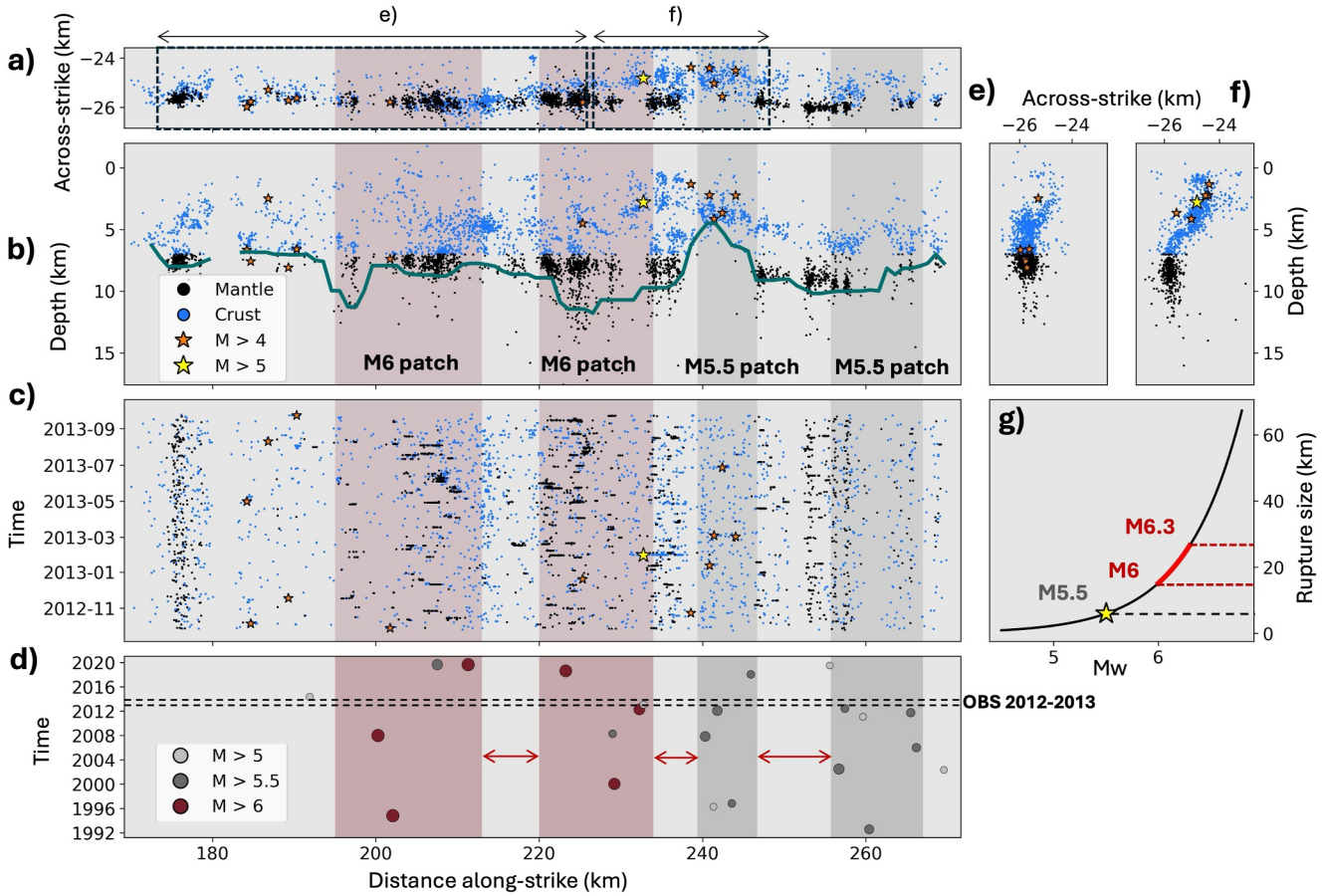

Figure 9. Along-strike segmentation, rupture patches, and seismicity patterns along the Blanco Ridge segment. (a), (b) and (c) shows across-strike, along-depth and the time evolution, respectively, of earthquakes distribution as a function of their along-strike projection along the BR segment. Black and blue dots show mantle and crustal microseismicity, respectively, while orange and yellow stars represent earthquake with a local magnitude greater than 4 and 5, respectively. Vertical red and gray bands highlight along-strike segments associated with recurring M6 and M5.5 rupture patches, respectively. A vertical exaggeration of 1.5 is applied in (c). (d) Time versus along-strike distribution of $M_W \geq 5.5$ earthquakes from the long-term re-located catalog (1992–2020) of Shi et al. (2022), illustrating the persistence of two $M_W \sim 6$ asperities and adjacent $M_W \approx 5.5$ patches over multiple seismic cycles. Red arrows indicate rupture barriers between major rupture patches. Horizontal black dashed lines stand for the 2012–2013 OBS network lifetime. (e) and (f) show the across-strike versus. depth projection of earthquakes for two portions of the BR fault represented in (a). (g) Relation between rupture size and M_W according to de Melo et al. (2025).

4. Discussion

4.1. Hydrothermal Controls on Step-Over Seismicity and Thermal Structure

A primary objective of this study is to understand how the space–time organization of microseismicity at step-overs reflects their thermal structure and dynamical regime, ranging from magma-poor pull-apart basins to fully developed ITSCs. A first-order feature of our observations is that earthquake density is strongly concentrated at step-overs relative to the intervening transform segments, indicating that these structures act as persistent loci of strain localization and seismic release. Our high-resolution earthquake catalog further reveals variations in the maximum depth, vertical extent, and temporal clustering of seismicity across the four major step-overs of the BTF (EBD, SUD, CAD, and GD), suggesting that these structures do not share a uniform thermal state.

To evaluate the thermal conditions required to explain the observed depth distribution of seismicity at CAD, we compare earthquake locations with three end-member thermal configurations (Figure 5a). Seismicity extends to ∼10 km depth across most of the CAD system, and locally reaches ∼13 km depth in its northeastern sector, indicating a significantly deeper brittle–ductile transition than expected for a fully magmatic spreading center. A half-space cooling model, which fully resets the thermal structure and places the 600°C isotherm near the surface, fails to reproduce this deep seismicity. In contrast, the BTF-calibrated 0-ITSC model developed in this study predicts a brittle–ductile transition near ∼13 km depth, consistent with the deepest observed earthquakes, while

the 1-ITSC model of Chen et al. (2025), which places the 600°C isotherm around ∼10 km depth, explains the majority of the CAD seismicity. Together, these results indicate that CAD is unlikely to behave as a fully magmatic or strongly thermally reset ITSC, and is instead more consistent with a magma-poor system whose thermal structure is primarily controlled by efficient hydrothermal cooling.

A further first-order feature of our observations is that seismicity at step-overs consists of quasi-continuous background microseismicity, with superimposed space–time clusters forming repeated seismic bursts of earthquakes over short time intervals. Dredged rocks and mineralogical studies beneath the East Blanco and Gorda depressions reveal extensive seawater infiltration and hydrothermal alteration, indicating active low-temperature hydrothermal circulation at EBD and high-temperature hydrothermal mineralization at GD (Gartman & Hein, 2019; Hart et al., 1990; Hein et al., 1999; James et al., 2008). The extensional tectonic geometry of pull-apart basins, characterized by high crustal permeability associated with normal faulting, facilitates long-lived hydrothermal circulation and the development of hydraulically connected fault–fracture networks, which likely sustain quasi-continuous background seismicity. Superimposed on this background, transient fluid pressure fluctuations within these networks may promote episodic rupture, resulting in swarm-like earthquake sequences (Masoch et al., 2025).

Previous studies interpreted deep mantle seismicity beneath CAD as reflecting rapidly cooling, intermittent magma intrusions sourced from depth (Kuna, 2020), while seismic tomography revealed low-V_s anomalies consistent with partial melting in the mantle between ∼16 and 22 km depth (Adimah et al., 2024). Together, these observations indicate that melt is present beneath CAD but remains confined to depth and does not sustain long-lived magmatic accretion at the surface. In this context, our observations of deep seismicity and recurrent seismic bursts suggest that CAD behaves as a nascent, magma-poor ITSC, in which episodic magma injections interact with a highly permeable, hydrothermally cooled lithosphere, triggering transient swarms of brittle failure in the lower crust and upper mantle without producing a fully developed spreading center. This behavior is consistent with a type-II step-over classification (Wolfson-Schwehr et al., 2017), in which partial thermal resetting occurs within a nascent ITSC.

Although Ren et al. (2023) interpreted the East Blanco Depression (EBD) as a remnant, aborted rift structure that did not evolve into a fully developed ITSC, multiple lines of evidence suggest that EBD may represent a more thermally and dynamically active system. Our OBS data reveal repeated space–time clusters of microseismicity at EBD, indicating persistent episodic strain release similar to that observed at CAD. Seismo-acoustic observations further documented intense earthquake swarms accompanied by long-duration, low-frequency tremor-like signals at EBD, interpreted as volcanogenic and associated with magma intrusion at depth (Dziak et al., 1996). While low-V_s anomalies imaged in regional tomography suggest the presence of partial melt at mantle depths (Adimah et al., 2024), an active hydrothermal system is inferred at shallower crustal levels (Gartman & Hein, 2019; Hein et al., 1999; James et al., 2008). In addition, thermo-mechanical modeling by Chen et al. (2025) shows that a partially reset thermal structure in West Blanco, including an ITSC at EBD, provides a first-order match to the observed seismicity distribution. Together, these observations suggest that EBD occupies a transitional thermal and dynamical regime between a magma-poor pull-apart basin (step-over type III) and an ITSC type II, following the framework of Wolfson-Schwehr et al. (2017).

The comparison between observed maximum earthquake depths and multiple thermo-mechanical configurations highlights the central role of hydrothermal circulation in shaping the thermal structure of step-overs (Figure 5). Rather than requiring pervasive magmatic heating or uniformly reset thermal fields, the observed depth extent of seismicity is broadly consistent with a lithosphere whose thermal structure is locally modified by variable hydrothermal efficiency. This finding supports a view in which Blanco step-overs are governed by a balance between limited magmatic input, fault-controlled permeability, and fluid-mediated cooling, leading to heterogeneous thermal states along strike.

4.2. Along-Strike Variability in Slip Behavior Along the Blanco Ridge Segment

A central motivation of this section is to understand how seismic coupling and slip modes vary along the BR segment by integrating short-term microseismic observations with the long-term seismic history of the fault. By calibrating the global $M > 5.5$ oceanic transform fault catalog of Shi et al. (2022) with the M_W 5.5 earthquake recorded on BR in January 2013, we refine the along-strike locations of the two quasi-periodic $M_W \sim 6$ asperities previously identified on BR. A key result of our analysis is that these two locked asperities spatially coincide with

the most active and persistent mantle swarm zones observed during the 2012–2013 OBS deployment. These regions host the highest density of deep microseismicity and exhibit repeated swarm activity.

One plausible interpretation of this spatial correlation is that repeated large earthquakes on the BR progressively damage and fracture the overlying crust, enhancing permeability and promoting long-term seawater infiltration along the fault zone. Over geological timescales, sustained fluid circulation may facilitate hydrothermal alteration of the upper mantle, leading to localized serpentinization beneath the most strongly coupled crustal asperities. Consistent with this interpretation, seismic velocity models of Adimah et al. (2024) reveal low-V_s anomalies beneath the two most active mantle swarm zones along BR, corresponding to an estimated 13%–25% degree of serpentinization in the upper mantle. These swarm zones are located above our inferred ~500°C isotherm (around 8 km depth), consistent with the lower thermal stability limit of antigorite under oceanic transform fault conditions (Guillot et al., 2015; Prigent et al., 2020; Cox et al., 2021; Z. Wang et al., 2022), supporting the plausibility of serpentinized mantle pockets at these depths.

Between the two $M \sim 6$ asperities, a persistent rupture barrier is evident across timescales. This barrier is expressed in the long-term catalog as a sustained deficit of large earthquakes and, in the short-term OBS catalog, as a zone of reduced mantle microseismicity. The stability of this feature over multiple earthquake cycles suggests long-lived mechanical segmentation, in which localized locked asperities rupture episodically while the intervening region primarily accommodates strain aseismically. The coexistence of microseismic activity with a lack of large ruptures indicates that the barrier does not represent a mechanically inactive zone, but rather one characterized by distributed deformation and limited rupture propagation. We note, however, that the OBS deployment occurred only a few months after a major $M \sim 6$ rupture on the eastern asperity, and thus captures the barrier during a potentially transient postseismic phase, which may contribute to the relatively low microseismicity rates observed during the experiment (Gong et al., 2026).

A second potential rupture barrier is inferred southeast of the eastern $M \sim 6$ asperity, separating this locked patch from a $M_W \approx 5.5$ rupture patch further east. Unlike the central barrier, this zone is characterized by elevated levels of both crustal and mantle seismicity, including recurrent swarm-like activity in the short-term OBS catalog. Across-strike projections reveal a systematic northeastward offset of crustal seismicity by approximately 1.5 km, indicating localized fault bending and increased structural complexity in this section of the transform (Figures 9e and 9f). This geometric irregularity, combined with the presence of active deep seismicity, suggests that this barrier may act as a mechanical discontinuity that inhibits rupture propagation from the eastern $M \sim 6$ asperity toward the adjacent $M_W \approx 5.5$ patch.

In contrast to the M6 locked patches in western BR, we observe an absence of upper-mantle seismic bursts beneath the M5.5 patches in the eastern segment. As shown in Figure 9g, a M5.5 earthquake corresponds to a rupture length of 6 km, whereas M6–6.3 events typically rupture over 20 km at OTF (de Melo et al., 2025). This difference in rupture size (a factor of 3.5) may lead to substantially different levels of cumulative damage within the fault zone over time. In turn, this could influence the degree of hydrothermal alteration of the underlying upper mantle, and consequently the occurrence of upper-mantle microseismicity.

The depth extent of mantle seismicity increases eastward along BR, from approximately 8 km in the western portion of the segment to nearly 10 km toward the eastern asperity. The observed along-strike deepening suggests localized cooling or rheological heterogeneity that allows brittle failure to persist at greater depths in some portions of the segment.

4.3. Limits and Perspectives

A primary limitation of this study concerns the interpretation of absolute earthquake depths and the comparison with previously published catalogs derived from the same OBS data set. While the comparison with studies such as Kuna (2020), M. Liu and Tan (2024), and Lange et al. (2026) is informative, direct quantitative comparison is inherently challenging because each approach relies on different phase selection criteria, picking strategies, velocity models, and relocation workflows. As a result, discrepancies in inferred maximum earthquake depths may reflect methodological choices rather than true physical differences. In particular, earthquake depth estimates are sensitive to assumptions about the velocity structure and to the treatment of three-dimensional heterogeneity.

A second limitation concerns the resolution of the subsurface thermal and rheological structure. While comparisons with thermo-mechanical models and phase stability constraints provide indirect evidence for

hydrothermal cooling and localized serpentinization, the true three-dimensional thermal structure of the BTF and its step-overs remains imperfectly resolved. In particular, uncertainties in crustal thickness, sediment distribution, and lateral velocity heterogeneity may influence earthquake depth estimates and the inferred position of isotherms. Future high-resolution seismic imaging, including local seismic velocity tomography using the machine-learning-derived catalog presented here, would be useful for further investigating variations in temperature, alteration, and melt content beneath step-overs and along the BR segment.

Finally, the temporal coverage of the OBS deployment represents an inherent limitation for interpreting slip behavior over the full seismic cycle. The 2012–2013 experiment captures only a short snapshot of microseismic activity relative to the ∼13-year recurrence interval of $M \sim 6$ earthquakes on BR. As a result, the observed space–time patterns of mantle swarms and rupture barrier behavior may not fully represent their average state over an entire interseismic cycle. Targeted future OBS deployments, particularly across key structures such as CAD, EBD, and the BR asperities, would enable direct observation of temporal variability in mantle seismicity, fluid-driven swarms, and barrier dynamics. Deployments spanning a large ($M \sim 6$) earthquake at BR would be especially valuable for constraining how mantle creep, hydrothermal processes, and rupture segmentation interact through the seismic cycle.

5. Conclusions

We present a high-resolution earthquake catalog derived from the 2012–2013 X9 OBS deployment across the BTF, nearly doubling the number of detected events relative to previous studies. This catalog reveals detailed patterns of seismic depth, space–time clustering, and fault segmentation that allow us to further constrain the thermal and mechanical structure of step-overs and the slip behavior of the BR segment.

Comparisons between observed maximum earthquake depths and multiple thermo-mechanical configurations indicate that hydrothermal circulation exerts a first-order control on the thermal structure of step-overs along the BTF. The CAD is best explained as a magma-poor, nascent ITSC characterized by partial thermal resetting and efficient hydrothermal cooling, as reflected by deep seismicity and recurrent seismic bursts. At the EBD, the combined evidence from hydrothermal mineralization, seismo-acoustic detections of volcanic tremor, and pronounced space–time clustering of microseismicity is consistent with an active hydrothermal system that may be episodically influenced by transient magma input, without requiring sustained magmatic accretion.

Along the BR, the comparison of short-term microseismicity with the long-term $M > 5.5$ earthquake record refines the locations of two quasi-periodic $M_W \sim 6$ asperities and reveals strong along-strike variability in slip behavior. The three most active mantle swarm zones are spatially colocated beneath these two locked asperities, as well as beneath a smaller rupture barrier separating the eastern $M_W \sim 6$ asperity from an adjacent $M_W \approx 5.5$ rupture patch, where crustal fault bending and structural complexity are observed. This spatial organization indicates vertically coupled deformation in which brittle crustal rupture, episodic mantle creep, and localized structural heterogeneity jointly control slip partitioning along the BR segment.

Conflict of Interest

The authors declare no conflicts of interest relevant to this study.

Availability Statement

Continuous seismic data were accessed from the NSF NGF data archive operated by EarthScope Consortium (NSF award 2435260). The OBS deployment X9 (2012–2013) data are available through the International Federation of Digital Seismograph Networks under network code X9 at Nabelek and Braunmiller (2012). We used the PickBlue OBS picker from SeisBench, available at Münchmeyer et al. (2023). Our final earthquake catalog from this study, CNN phase picker model BlancOBS, and thermal model are available at Journeau et al. (2026) with headers description in Text S2 in Supporting Information S1. The bathymetry was downloaded from the Global Multi-Resolution Topography database (GMRT), at www.gmrt.org (Ryan et al., 2009).

Acknowledgments
This material is based upon work supported by the U.S. Geological Survey under Grants G22AP00299 and G22AP00300 and by the National Science Foundation Award 1848302. We thank all individuals and organizations who contributed to data collection in the Blanco Transform OBS experiment (Nabelek & Braunmiller, 2012). This work benefited from access to the University of Oregon high performance computing cluster, Talapas. We thank the editor Mark Behn and the associate editor for handling this manuscript. We thank Ingo Grevemeyer and two anonymous reviewers for helpful reviews that improved quality of this manuscript. We also thank Doug Toomey, Emilie Hooft, Sylvain Barbot, and Yu Ren for discussions on the Blanco Transform Fault.

References

Abercrombie, R. E., & Ekström, G. (2001). Earthquake slip on oceanic transform faults. *Nature*, *410*(6824), 74–77. https://doi.org/10.1038/35065064

Adimah, N. I., Tan, Y. J., & Russell, J. B. (2024). Shear-wave velocity structure of the Blanco oceanic transform fault zone. *Geophysical Journal International*, *239*(2), 1287–1312. https://doi.org/10.1093/gji/ggae318

Aki, K. (1965). Maximum likelihood estimate of b in the formula log n=a-bm and its confidence limits. *Bull. Earthquake Res. Inst., Tokyo Univ.*, *43*, 237–239. Retrieved from https://cir.nii.ac.jp/crid/1573387450038851840

Bakun, W. H., & Joyner, W. B. (1984). The ML scale in central California. *Bulletin of the Seismological Society of America*, *74*(5), 1827–1843. https://doi.org/10.1785/BSSA0740051827

Behn, M. D., Boettcher, M. S., & Hirth, G. (2007). Thermal structure of oceanic transform faults. *Geology*, *35*(4), 307–310. https://doi.org/10.1130/G23112A.1

Bender, B. (1983). Maximum likelihood estimation of b values for magnitude grouped data. *Bulletin of the Seismological Society of America*, *73*(3), 831–851. https://doi.org/10.1785/BSSA0730030831

Beyreuther, M., Barsch, R., Krischer, L., Megies, T., Behr, Y., & Wassermann, J. (2010). ObsPy: A python toolbox for seismology. *Seismological Research Letters*, *81*(3), 530–533. https://doi.org/10.1785/gssrl.81.3.530

Boettcher, M. S., Hirth, G., & Evans, B. (2007). Olivine friction at the base of oceanic seismogenic zones. *Journal of Geophysical Research*, *112*(B1), B01205. https://doi.org/10.1029/2006JB004301

Boettcher, M. S., & Jordan, T. H. (2004). Earthquake scaling relations for mid-ocean ridge transform faults. *Journal of Geophysical Research*, *109*(B12). https://doi.org/10.1029/2004JB003110

Boettcher, M. S., & McGuire, J. J. (2009). Scaling relations for seismic cycles on mid-ocean ridge transform faults. *Geophysical Research Letters*, *36*(21). https://doi.org/10.1029/2009GL040115

Bornstein, T., Lange, D., Münchmeyer, J., Woollam, J., Rietbrock, A., Barcheck, G., et al. (2024). Pickblue: Seismic phase picking for ocean bottom seismometers with deep learning. *Earth and Space Science*, *11*(1), e2023EA003332. https://doi.org/10.1029/2023EA003332

Braunmiller, J., & Nábělek, J. (2008). Segmentation of the blanco transform fault zone from earthquake analysis: Complex tectonics of an oceanic transform fault. *Journal of Geophysical Research*, *113*(B7). https://doi.org/10.1029/2007JB005213

Chen, Z., Zhang, F., Zha, C., Liu, S., Zhou, Z., Lin, J., et al. (2025). Important role of intra-transform spreading centers in shaping thermal structure along the blanco transform fault. *Journal of Earth Science*. https://doi.org/10.1007/s12583-025-0293-3

Chesley, C., Evans, R., Warren, J. M., Gase, A. C., Perez, J., Armerding, C., et al. (2025). Evidence for crustal brines and deep fluid infiltration in an oceanic transform fault. *Science Advances*, *11*(15), eadu3661. https://doi.org/10.1126/sciadv.adu3661

Christeson, G. L., Karson, J. A., & McIntosh, K. D. (2010). Mapping of seismic layer 2a/2b boundary above the sheeted dike unit at intermediate spreading crust exposed near the blanco transform. *Geochemistry, Geophysics, Geosystems*, *11*(3). https://doi.org/10.1029/2009GC002864

Cox, S., Ikari, M. J., MacLeod, C. J., & Åke, F. (2021). Frictional characteristics of oceanic transform faults: Progressive deformation and alteration controls seismic style. *Geophysical Research Letters*, *48*(24), e2021GL096292. https://doi.org/10.1029/2021GL096292

Deichmann, N. (2017). Theoretical basis for the observed break in ml/mw scaling between small and large earthquakes. *Bulletin of the Seismological Society of America*, *107*(2), 505–520. https://doi.org/10.1785/0120160318

de Melo, G. W. S., Grevemeyer, I., Lange, D., Metz, D., & Kopp, H. (2025). Relationship between rupture length and magnitude of oceanic transform fault earthquakes. *Geophysical Research Letters*, *52*(1), e2024GL112891. https://doi.org/10.1029/2024GL112891

DeMets, C., Gordon, R. G., & Argus, D. F. (2010). Geologically current plate motions. *Geophysical Journal International*, *181*(1), 1–80. https://doi.org/10.1111/j.1365-246X.2009.04491.x

Dziak, R. P., Fox, C. G., & Embley, R. W. (1991). Relationship between the seismicity and geologic structure of the blanco transform fault zone. *Marine Geophysical Researches*, *13*(3), 203–208. https://doi.org/10.1007/BF00369149

Dziak, R. P., Fox, C. G., Embley, R. W., Lupton, J. E., Johnson, G. C., Chadwick, W. W., & Koshi, R. A. (1996). Detection of and response to a probable volcanogenic t-wave event swarm on the Western blanco transform fault zone. *Geophysical Research Letters*, *23*(8), 873–876. https://doi.org/10.1029/96GL00240

Dziak, R. P., Fox, C. G., Embley, R. W., Nabelek, J. L., Braunmiller, J., & Koski, R. A. (2000). Recent tectonics of the blanco ridge, eastern blanco transform fault zone. *Marine Geophysical Researches*, *21*(5), 423–450. https://doi.org/10.1023/A:1026545910893

Embley, R. W., & Wilson, D. S. (1992). Morphology of the blanco transform fault zone-ne Pacific: Implications for its tectonic evolution. *Marine Geophysical Researches*, *14*(1), 25–45. https://doi.org/10.1007/BF01674064

Fan, W., McGuire, J. J., Liu, Y., Behn, M. D., Warren, J. M., Collins, J. A., & Boettcher, M. S. (2026). Dynamics of rupture barriers on oceanic transform faults: Insights from the westernmost gofar transform fault. *Journal of Geophysical Research: Solid Earth*, *131*(5), e2025JB033439. https://doi.org/10.1029/2025JB033439

Fox, P. J., & Gallo, D. G. (1984). A tectonic model for ridge-transform-ridge plate boundaries: Implications for the structure of oceanic lithosphere. *Tectonophysics*, *104*(3–4), 205–242. https://doi.org/10.1016/0040-1951(84)90124-0

Froment, B., McGuire, J. J., van der Hilst, R. D., Gouédard, P., Roland, E. C., Zhang, H., & Collins, J. A. (2014). Imaging along-strike variations in mechanical properties of the gofar transform fault, east Pacific rise. *Journal of Geophysical Research: Solid Earth*, *119*(9), 7175–7194. https://doi.org/10.1002/2014JB011270

Gartman, A., & Hein, J. R. (2019). Chapter 5 - Mineralization at oceanic transform faults and fracture zones. In J. C. Duarte (Ed.), *Transform plate boundaries and fracture zones* (pp. 105–118). Elsevier. https://doi.org/10.1016/B978-0-12-812064-4.00005-0

Gong, J., & Fan, W. (2022). Seismicity, fault architecture, and slip mode of the westernmost gofar transform fault. *Journal of Geophysical Research: Solid Earth*, *127*(11), e2022JB024918. https://doi.org/10.1029/2022JB024918

Gong, J., Fan, W., McGuire, J. J., Behn, M. D., Warren, J. M., Roland, E., et al. (2026). Predictable seismic cycles result from structural rupture barriers on oceanic transform faults. *Science*. *392*(6799), 718–723. https://doi.org/10.1126/science.ady6190

Gong, J., Fan, W., & Parnell-Turner, R. (2022). Microseismicity indicates atypical small-scale plate rotation at the quebrada transform fault system, east Pacific rise. *Geophysical Research Letters*, *49*(3), e2021GL097000. https://doi.org/10.1029/2021GL097000

Gong, J., Fan, W., & Parnell-Turner, R. (2023). Machine learning-based new earthquake catalog illuminates on-fault and off-fault seismicity patterns at the discovery transform fault, east Pacific rise. *Geochemistry, Geophysics, Geosystems*, *24*(9), e2023GC011043. https://doi.org/10.1029/2023GC011043

Grevemeyer, I., Hayman, N. W., Lange, D., Peirce, C., Papenberg, C., Van Avendonk, H. J., et al. (2019). Constraining the maximum depth of brittle deformation at slow- and ultraslow-spreading ridges using microseismicity. *Geology*, *47*(11), 1069–1073. https://doi.org/10.1130/G46577.1

Guillot, S., Schwartz, S., Reynard, B., Agard, P., & Prigent, C. (2015). Tectonic significance of serpentinites. *Tectonophysics*, *646*, 1–19. https://doi.org/10.1016/j.tecto.2015.01.020

Guo, H., Zhang, H., & Froment, B. (2018). Structural control on earthquake behaviors revealed by high-resolution vp/vs imaging along the gofar transform fault, east Pacific rise. *Earth and Planetary Science Letters*, *499*, 243–255. https://doi.org/10.1016/j.epsl.2018.07.037

Hanks, T. C., & Boore, D. M. (1984). Moment-magnitude relations in theory and practice. *Journal of Geophysical Research*, *89*(B7), 6229–6235. https://doi.org/10.1029/JB089iB07p06229

Hanks, T. C., & Kanamori, H. (1979). A moment magnitude scale. *Journal of Geophysical Research*, *84*(B5), 2348–2350. https://doi.org/10.1029/JB084iB05p02348

Hart, R., Hoefs, J., & Pyle, D. (1990). Multistage hydrothermal systems in the blanco fracture zone. In G. R. McMurray (Ed.), *Gorda ridge* (pp. 51–75). Springer New York.

Hein, J. R., Koski, R. A., Embley, R. W., Reid, J. A., & Chang, S.-W. (1999). Diffuse-flow hydrothermal field in an oceanic fracture zone setting, northeast Pacific; deposit composition. *Exploration and Mining Geology*, *8*(3–4), 299–322.

Hutton, L. K., & Boore, D. M. (1987). The ml scale in southern California. *Bulletin of the Seismological Society of America*, *77*(6), 2074–2094. https://doi.org/10.1785/BSSA0770062074

James, R., Hein, R. A. K. R. W. E., Clague, D. A., & Dunham, R. E. (2008). Metalliferous sediment and a silica-hematite deposit within the Blanco fracture zone, northeast Pacific. *Marine Georesources and Geotechnology*, *26*(4), 317–339. https://doi.org/10.1080/10641190802430986

Journeau, C., Thomas, A., Abercrombie, R., Hirao, B., Liu, M., & Kuna, V. (2026). Dataset for OBS data mining reveals seismic structure and dynamics of the Oceanic blanco transform fault, Northeast Pacific. *ZenodoJournal of Geophysical Research - Solid Earth*. [Dataset]. https://doi.org/10.5281/zenodo.18501127

Kuna, V. M. (2020). Investigation of slip and tectonics of the Blanco transform fault using high-resolution ocean bottom seismic data (dissertation). *Oregon State University, College of Earth, Ocean, and Atmospheric Sciences*.

Kuna, V. M., & Nábělek, J. L. (2021). Seismic crustal imaging using fin whale songs. *Science*, *371*(6530), 731–735. https://doi.org/10.1126/science.abf3962

Kuna, V. M., Nábělek, J. L., & Braunmiller, J. (2019). Mode of slip and crust–mantle interaction at oceanic transform faults. *Nature Geoscience*, *12*(2), 138–142. https://doi.org/10.1038/s41561-018-0287-1

Lange, D., Ren, Y., & Grevemeyer, I. (2026). Seismicity, repeating earthquakes, and tomographic imaging of the Blanco transform fault system, northeast Pacific. *Journal of Geophysical Research: Solid Earth*, *131*(5), e2025JB031584. https://doi.org/10.1029/2025JB031584

Liu, M., & Barbot, S. (2026). Role of hydrothermal alteration and thermally activated healing on earthquake dynamics along oceanic transform faults. *Earth and Planetary Science Letters*, *675*, 119765. https://doi.org/10.1016/j.epsl.2025.119765

Liu, M., Gerya, T., & Rozel, A. (2025). The effect of brittle-ductile weakening on the formation of faulting patterns at mid-ocean ridges. *Tectonics*, *44*(2), e2024TC008586. https://doi.org/10.1029/2024TC008586

Liu, M., Gerya, T., & Rozel, A. B. (2022). Self-organization of magma supply controls crustal thickness variation and tectonic pattern along melt-poor mid-ocean ridges. *Earth and Planetary Science Letters*, *584*, 117482. https://doi.org/10.1016/j.epsl.2022.117482

Liu, M., & Tan, Y. J. (2024). Evaluating the performance of machine-learning-based phase pickers when applied to ocean bottom seismic data: Blanco oceanic transform fault as a case study. Retrieved from https://arxiv.org/abs/2410.18041

Liu, M., & Tan, Y. J. (2025). Evaluating the performance of machine-learning-based phase pickers when applied to ocean bottom seismic data: Blanco oceanic transform fault as a case study. *Geophysical Journal International*, *242*(3), ggaf256. https://doi.org/10.1093/gji/ggaf256

Liu, T., Gong, J., Fan, W., & Lin, G. (2023). In-situ vp/vs reveals fault-zone material variation at the westernmost gofar transform fault, east pacific rise. *Journal of Geophysical Research: Solid Earth*, *128*(3), e2022JB025310. https://doi.org/10.1029/2022JB025310

Lomax, A., Michelini, A., & Curtis, A. (2009). Earthquake location, direct, global-search methods. In R. A. Meyers (Ed.), *Encyclopedia of complexity and systems science* (pp. 1–33). Springer New York. https://doi.org/10.1007/978-3-642-27737-5_150-2

Lomax, A., & Savvaidis, A. (2022). High-precision earthquake location using source-specific station terms and inter-event waveform similarity. *Journal of Geophysical Research: Solid Earth*, *127*(1), e2021JB023190. https://doi.org/10.1029/2021JB023190

Lomax, A., Virieux, J., Volant, P., & Berge-Thierry, C. (2000). Probabilistic earthquake location in 3d and layered models. In C. H. Thurber & N. Rabinowitz (Eds.), *Advances in seismic event location* (pp. 101–134). Springer Netherlands. https://doi.org/10.1007/978-94-015-9536-0_5

Masoch, S., Pennacchioni, G., Fondriest, M., Gomila, R., Poli, P., Cembrano, J., & Di Toro, G. (2025). Earthquake swarms frozen in an exhumed hydrothermal system (Bolfin fault zone, chile). *Solid Earth*, *16*(1), 23–43. https://doi.org/10.5194/se-16-23-2025

McGuire, J. J., Collins, J. A., Gouédard, P., Roland, E., Lizarralde, D., Boettcher, M. S., et al. (2012). Variations in earthquake rupture properties along the gofar transform fault, east Pacific rise. *Nature Geoscience*, *5*(5), 336–341. https://doi.org/10.1038/ngeo1454

Michele, M., Latorre, D., & Emolo, A. (2019). An empirical formula to classify the quality of earthquake locations. *Bulletin of the Seismological Society of America*, *109*(6), 2755–2761. https://doi.org/10.1785/0120190144

Molnar, P. (2020). The brittle-plastic transition, earthquakes, temperatures, and strain rates. *Journal of Geophysical Research: Solid Earth*, *125*(7), e2019JB019335. https://doi.org/10.1029/2019JB019335

Mousavi, S. M., Ellsworth, W. L., Zhu, W., Chuang, L. Y., & Beroza, G. C. (2020). Earthquake Transformer—an attentive deep-learning model for simultaneous earthquake detection and phase picking. *Nature Communications*, *11*(1), 3952. https://doi.org/10.1038/s41467-020-17591-w

Münchmeyer, J. (2024). Pyocto: A high-throughput seismic phase associator. *Seismica*, *3*(1). https://doi.org/10.26443/seismica.v3i1.1130

Münchmeyer, J., jawooll, J., Bornstein, T., Chamberlain, C., Saul, J., Zhu, J., et al. (2023). SeisBench v0.4 – Bringing SeisBench to the ocean bottom. *Zenodo*. [Software]. https://doi.org/10.5281/zenodo.7828105

Münchmeyer, J., Woollam, J., Rietbrock, A., Tilmann, F., Lange, D., Bornstein, T., et al. (2022). Which picker fits my data? A quantitative evaluation of deep learning based seismic pickers. *Journal of Geophysical Research: Solid Earth*, *127*(1), e2021JB023499. https://doi.org/10.1029/2021JB023499

Nabelek, J. L., & Braunmiller, J. (2012). Plate boundary evolution and physics at an oceanic transform fault system. *International Federation of Digital Seismograph Networks*. https://doi.org/10.7914/SN/X9_2012

Prigent, C., Warren, J., Kohli, A., & Teyssier, C. (2020). Fracture-mediated deep seawater flow and mantle hydration on oceanic transform faults. *Earth and Planetary Science Letters*, *532*, 115988. https://doi.org/10.1016/j.epsl.2019.115988

Ren, Y., Lange, D., & Grevemeyer, I. (2023). Seismotectonics of the blanco transform fault system, northeast pacific: Evidence for an immature plate boundary. *Journal of Geophysical Research: Solid Earth*, *128*(3), e2022JB026045. https://doi.org/10.1029/2022JB026045

Roland, E., Behn, M. D., & Hirth, G. (2010). Thermal-mechanical behavior of oceanic transform faults: Implications for the spatial distribution of seismicity. *Geochemistry, Geophysics, Geosystems*, *11*(7), Q07001. https://doi.org/10.1029/2010GC003034

Roland, E., Lizarralde, D., McGuire, J. J., & Collins, J. A. (2012). Seismic velocity constraints on the material properties that control earthquake behavior at the quebrada-discovery-gofar transform faults, east Pacific rise. *Journal of Geophysical Research*, *117*(B11), B11102. https://doi.org/10.1029/2012JB009422

Ryan, W. B. F., Carbotte, S. M., Coplan, J. O., O'Hara, S., Melkonian, A., Arko, R., et al. (2009). Global multi-resolution topography synthesis. *Geochemistry, Geophysics, Geosystems*, *10*(3). https://doi.org/10.1029/2008GC002332

Schlaphorst, D., Rychert, C. A., Harmon, N., Hicks, S. P., Bogiatzis, P., Kendall, J.-M., & Abercrombie, R. E. (2023). Local seismicity around the chain transform fault at the mid-atlantic ridge from obs observations. *Geophysical Journal International*, *234*(2), 1111–1124. https://doi.org/10.1093/gji/ggad124

Shi, P., Wei, M. M., & Pockalny, R. A. (2022). The ubiquitous creeping segments on oceanic transform faults. *Geology*, *50*(2), 199–204. https://doi.org/10.1130/G49562.1

Straume, E. O., Gaina, C., Medvedev, S., Hochmuth, K., Gohl, K., Whittaker, J. M., et al. (2019). Globsed: Updated total sediment thickness in the world's oceans. *Geochemistry, Geophysics, Geosystems*, *20*(4), 1756–1772. https://doi.org/10.1029/2018GC008115

Wang, K., Waldhauser, F., Schaff, D., Tolstoy, M., Wilcock, W. S. D., & Tan, Y. J. (2024). Real-time detection of volcanic unrest and eruption at axial seamount using machine learning. *Seismological Research Letters*, *95*(5), 2651–2662. https://doi.org/10.1785/0220240086

Wang, K., Waldhauser, F., Tolstoy, M., Schaff, D., Sawi, T., Wilcock, W. S. D., & Tan, Y. J. (2024). Volcanic precursor revealed by machine learning offers new eruption forecasting capability. *Geophysical Research Letters*, *51*(19), e2024GL108631. https://doi.org/10.1029/2024GL108631

Wang, Z., Singh, S. C., Prigent, C., Gregory, E. P. M., & Marjanović, M. (2022). Deep hydration and lithospheric thinning at oceanic transform plate boundaries. *Nature Geoscience*, *15*(9), 741–746. https://doi.org/10.1038/s41561-022-01003-3

White, M. C. A., Fang, H., Nakata, N., & Ben-Zion, Y. (2020). Pykonal: A python package for solving the eikonal equation in spherical and cartesian coordinates using the fast marching method. *Seismological Research Letters*, *91*(4), 2378–2389. https://doi.org/10.1785/0220190318

Wiemer, S., & Wyss, M. (2000). Minimum magnitude of completeness in earthquake catalogs: Examples from Alaska, the Western United States, and Japan. *Bulletin of the Seismological Society of America*, *90*(4), 859–869. https://doi.org/10.1785/0119990114

Wilson, D. S. (1993). Confidence intervals for motion and deformation of the juan de fuca plate. *Journal of Geophysical Research*, *98*(B9), 16053–16071. https://doi.org/10.1029/93JB01227

Wolfson-Schwehr, M., & Boettcher, M. S. (2019). Chapter 2 - Global characteristics of oceanic transform fault structure and seismicity. In J. C. Duarte (Ed.), *Transform plate boundaries and fracture zones* (pp. 21–59). Elsevier. https://doi.org/10.1016/B978-0-12-812064-4.00002-5

Wolfson-Schwehr, M., Boettcher, M. S., & Behn, M. D. (2017). Thermal segmentation of mid-ocean ridge-transform faults. *Geochemistry, Geophysics, Geosystems*, *18*(9), 3405–3418. https://doi.org/10.1002/2017GC006967

Wolfson-Schwehr, M., Boettcher, M. S., McGuire, J. J., & Collins, J. A. (2014). The relationship between seismicity and fault structure on the discovery transform fault, east Pacific rise. *Geochemistry, Geophysics, Geosystems*, *15*(9), 3698–3712. https://doi.org/10.1002/2014GC005445

Woollam, J., Münchmeyer, J., Tilmann, F., Rietbrock, A., Lange, D., Bornstein, T., et al. (2022). Seisbench—A toolbox for machine learning in seismology. *Seismological Research Letters*, *93*(3), 1695–1709. https://doi.org/10.1785/0220210324

Yu, Y., Ellsworth, W. L., & Beroza, G. C. (2024). Accuracy and precision of earthquake location programs: Insights from a synthetic controlled experiment. *Seismological Research Letters*, *96*(3), 1860–1874. https://doi.org/10.1785/0220240354

Zhu, W., & Beroza, G. C. (2018). Phasenet: A deep-neural-network-based seismic arrival-time picking method. *Geophysical Journal International*, *216*(1), 261–273. https://doi.org/10.1093/gji/ggy423